



## DEFENSE TECHNICAL INFORMATION CENTER

*Information for the Defense Community*

DTIC® has determined on 11 / 18 / 13 that this Technical Document has the Distribution Statement checked below. The current distribution for this document can be found in the DTIC® Technical Report Database.

☒ **DISTRIBUTION STATEMENT A.** Approved for public release; distribution is unlimited.

☐ **© COPYRIGHTED.** U.S. Government or Federal Rights License. All other rights and uses except those permitted by copyright law are reserved by the copyright owner.

☐ **DISTRIBUTION STATEMENT B.** Distribution authorized to U.S. Government agencies only (fill in reason) (date of determination). Other requests for this document shall be referred to (insert controlling DoD office).

☐ **DISTRIBUTION STATEMENT C.** Distribution authorized to U.S. Government Agencies and their contractors (fill in reason) (date determination). Other requests for this document shall be referred to (insert controlling DoD office).

☐ **DISTRIBUTION STATEMENT D.** Distribution authorized to the Department of Defense and U.S. DoD contractors only (fill in reason) (date of determination). Other requests shall be referred to (insert controlling DoD office).

☐ **DISTRIBUTION STATEMENT E.** Distribution authorized to DoD Components only (fill in reason) (date of determination). Other requests shall be referred to (insert controlling DoD office).

☐ **DISTRIBUTION STATEMENT F.** Further dissemination only as directed by (insert controlling DoD office) (date of determination) or higher DoD authority.

*Distribution Statement F is also used when a document does not contain a distribution statement and no distribution statement can be determined.*

☐ **DISTRIBUTION STATEMENT X.** Distribution authorized to U.S. Government Agencies and private individuals or enterprises eligible to obtain export-controlled technical data in accordance with DoDD 5230.25; (date of determination). DoD Controlling Office is (insert controlling DoD office).

REPORT DOCUMENTATION PAGE				Form Approved OMB No. 0704-0188	
<p>The public reporting burden for this collection of information is estimated to average 1 hour per response, including the time for reviewing instructions, searching existing data sources, gathering and maintaining the data needed, and completing and reviewing the collection of information. Send comments regarding this burden estimate or any other aspect of this collection of information, including suggestions for reducing the burden, to Department of Defense, Washington Headquarters Services, Directorate for Information Operations and Reports (0704-0188), 1215 Jefferson Davis Highway, Suite 1204, Arlington, VA 22202-4302. Respondents should be aware that notwithstanding any other provision of law, no person shall be subject to any penalty for failing to comply with a collection of information if it does not display a currently valid OMB control number.</p> <p><b>PLEASE DO NOT RETURN YOUR FORM TO THE ABOVE ADDRESS.</b></p>					
1. REPORT DATE (DD-MM-YYYY) 30-06-2010		2. REPORT TYPE FINAL		3. DATES COVERED (From - To) May 2007 - May 2010	
4. TITLE AND SUBTITLE Effect of Structure on the Initiation and Ignition Chemistry of Energetic Ionic Liquids				5a. CONTRACT NUMBER	
				5b. GRANT NUMBER FA9550-07-1-0432	
				5c. PROGRAM ELEMENT NUMBER	
6. AUTHOR(S) Thomas A. Litzinger				5d. PROJECT NUMBER	
				5e. TASK NUMBER	
				5f. WORK UNIT NUMBER	
7. PERFORMING ORGANIZATION NAME(S) AND ADDRESS(ES) Pennsylvania State University University Park, PA 16802				8. PERFORMING ORGANIZATION REPORT NUMBER	
9. SPONSORING/MONITORING AGENCY NAME(S) AND ADDRESS(ES) AFOSR/NA 875 N. Randolph St. Arlington, VA 22203				10. SPONSOR/MONITOR'S ACRONYM(S)	
				11. SPONSOR/MONITOR'S REPORT NUMBER(S)	
12. DISTRIBUTION/AVAILABILITY STATEMENT					
13. SUPPLEMENTARY NOTES					
14. ABSTRACT Ionic liquids are being explored to develop advanced propellants that provide higher performance and lower environmental impact than traditional propellant systems. Because of the flexibility in designing ionic liquids, both mono-propellants and bi-propellants are being pursued. A family of bi-propellant ionic liquids based on the dicyanamide ion have been developed that react hypergolically with white fuming nitric acid. The overall goal of this research program was to contribute to the fundamental understanding of the reactions of energetic ionic liquids by determining the effects of cation and anion structure on initiation reactions, and subsequent reactions leading to ignition, for representative compounds in three classes: amino-1,2,4 triazoles, amino-1,2,3-triazoles, and amino-tetrazoles. In order to achieve this objective, experiments were performed to determine the decomposition species and their temporal evolution over a range of temperatures. To gain further insight into the mechanism of decomposition, simplified kinetic models were formulated and overall kinetic parameters were derived. The second major research objective was to contribute to the understanding of the hypergolic reaction mechanism for the dicyanamide based ionic liquids.					
15. SUBJECT TERMS Ionic Liquids, Propellants, Hypergolic					
16. SECURITY CLASSIFICATION OF:			17. LIMITATION OF ABSTRACT	18. NUMBER OF PAGES	19a. NAME OF RESPONSIBLE PERSON
a. REPORT	b. ABSTRACT	c. THIS PAGE			19b. TELEPHONE NUMBER (Include area code)

## **Abstract**

Ionic liquids are being explored in the search for advanced propellants that provide higher performance and lower environmental impact than traditional propellant systems. Because of the flexibility in designing ionic liquids, both mono-propellants and bi-propellants are being pursued. A family of bi-propellant ionic liquids that react hypergolically with white fuming nitric acid was recently synthesized. The overall goal of this research program was to contribute to the fundamental understanding of the ignition of energetic ionic liquids by determining the effects of cation and anion structure on initiation reactions, and subsequent reactions leading to ignition, for representative compounds in three classes: amino-1,2,4 triazoles, amino-1,2,3-triazoles, and amino-tetrazoles. In order to achieve this objective, experiments were performed to determine the decomposition species and their temporal evolution over a range of temperatures. To gain further insight into the mechanism of decomposition, simplified kinetic models were formulated and overall kinetic parameters were derived. The second major research objective was to contribute to the understanding of the hypergolic reaction mechanism for the dicyanamide-based ionic liquids. Experimental results are reported for the species produced during hypergolic ignition as well as for the detection of a postulated key intermediate, dinitrobiuret.

## **1 RESEARCH OBJECTIVES**

The overall goal of this research program was to contribute to the fundamental understanding of the reactions of energetic ionic liquids (EIL) by determining the effects of cation ring structure and anion structure on initiation reactions, and subsequent reactions leading to ignition, for representative compounds in three classes: amino-1,2,4 triazoles, amino-1,2,3-triazoles, and amino-tetrazoles. In order to achieve this objective, experiments were performed to determine the decomposition species and their temporal evolution over a range of temperatures. To gain further insight into the mechanism of decomposition, simplified kinetic models were formulated and overall kinetic parameters were derived.

After the successful development of a hypergolic ionic liquid by the EIL team at Edwards, an additional research objective of verifying the reaction mechanism proposed by the Edwards team was added to the program.

## 2 EXPERIMENTAL METHODS

Two complementary experimental approaches were used in this program: Confined Rapid Thermolysis and Laser-induced Decomposition. The two experimental approaches along with their diagnostics involved are described in this section. In the studies of hypergolic ignition, two additional diagnostics were used: high temporal resolution imaging and rapid response thermocouple measurements.

### 2.1 Confined Rapid Thermolysis

In the confined rapid thermolysis (CRT)/FTIR/ToFMS studies, the thermal decomposition is limited to a volume confined between two heated, parallel surfaces. By using a small sample size compared to the volume, it is possible to study liquids that may otherwise largely boil off rather than decompose. The setup is composed of a constant pressure chamber, a Bruker IFS 66/S FTIR spectrometer and a commercially available ToF mass spectrometer. A three-dimensional view of the chamber, including a cut that exposes the sample holder, is shown in Figure 1. The sample holder is designed to be lifted by the bottom heater to enclose the sample between the two heaters. Two ports are provided on the chamber,

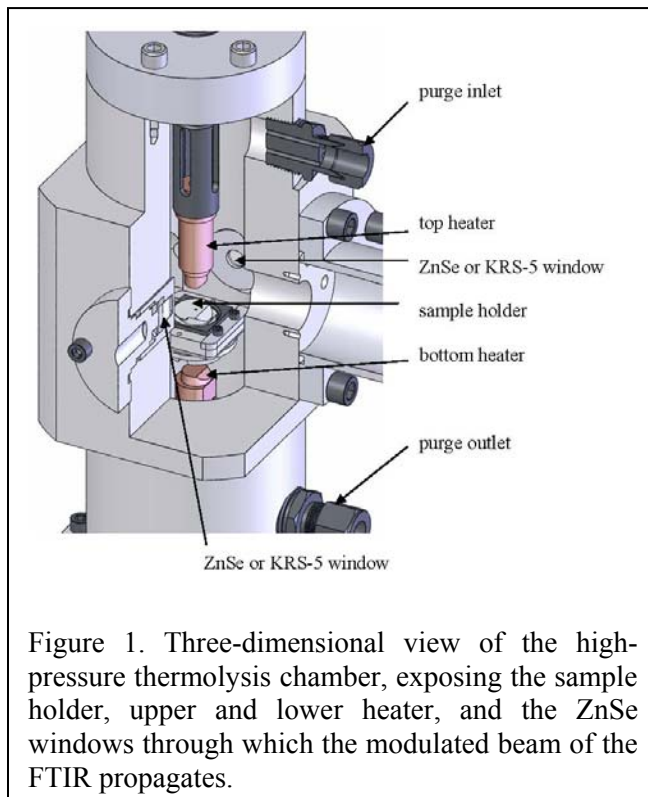
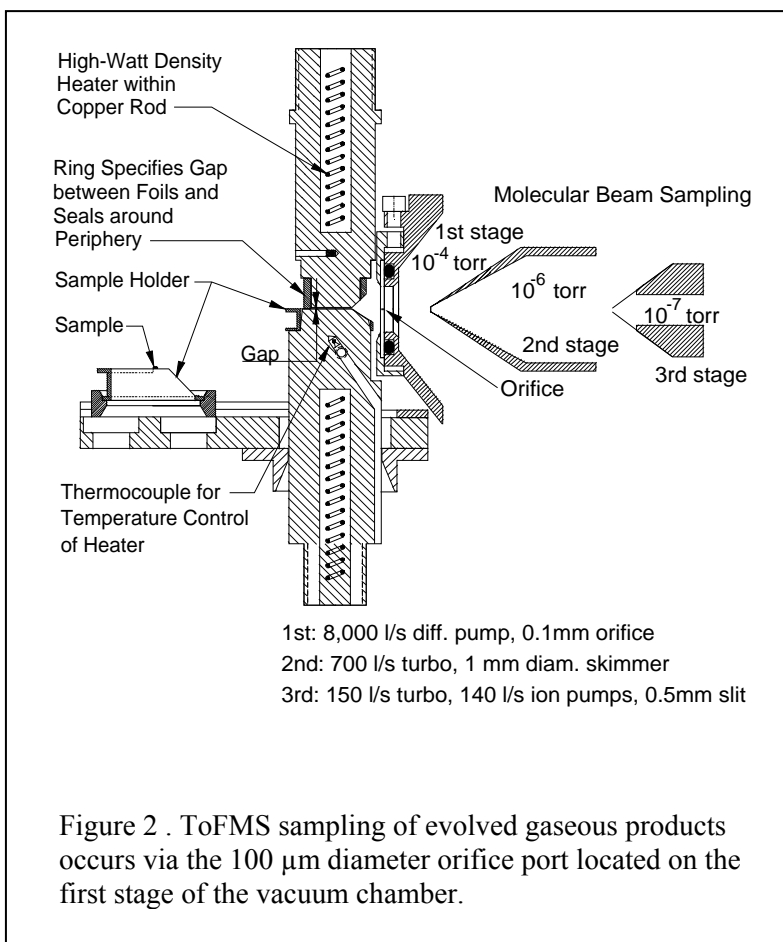


Figure 1. Three-dimensional view of the high-pressure thermolysis chamber, exposing the sample holder, upper and lower heater, and the ZnSe windows through which the modulated beam of the FTIR propagates.

one serves as an inlet to the purge gas and the other exhausts decomposition products and the purge gas stream. The constant pressure chamber, resting on a rigid frame, has a height of 27.5 cm and an inner diameter of 5 cm approximately. The CRT/FTIR technique has been described in detail in a previous work.<sup>1</sup>

The rapid thermolysis is achieved by using two heaters: a stationary top heater and a mobile bottom heater. The gases evolved during the thermolysis are detected, identified and quantified using FTIR transmission spectroscopy. The spectra are acquired with a spectral resolution of  $2\text{ cm}^{-1}$  and a temporal resolution of 50 ms. A non-linear, least squares method is utilized to extract the species concentrations of the evolved gases by comparison with theoretical transmittance<sup>2</sup>. After completion of the iterations, the relative concentrations of various species, such as  $\text{H}_2\text{O}$ ,  $\text{N}_2\text{O}$ ,  $\text{NO}_2$ ,  $\text{NO}$ ,  $\text{CO}_2$ , and  $\text{HNO}_3$  are obtained for each spectrum.

A low-pressure chamber with identical heater configurations is utilized for acquiring the ToF mass information. The ToF MS system (Model D-677 from R. M. Jordan) is equipped with a 1m flight tube and a 44 mm microchannel plate (MCP) detector. Here, the recharging of the MCP detector limits the temporal resolution to about 1 ms. Molecular beam sampling from atmospheric pressure gases is performed using a 100  $\mu\text{m}$  orifice plate attached to the first stage, a 1mm diameter Ni skimmer (manufactured in-house by electroplating) attached to the second stage and a vertically translatable 0.5 $\times$ 12mm<sup>2</sup> slit attached to the entrance of the third stage. A schematic is shown in Figure 2. Electron impact ionization is set at 70eV, resulting in fragmentation of molecules, but allowing comparison with mass spectral and related data bases<sup>3</sup>. Time-to-mass scaling is determined using the expressions  $m=a(t-t_0)^2$ , where the two constants for each mass spectrum are obtained from known positions of helium and argon.



## 2.2 Laser-driven Decomposition

Testing of materials for which gram-quantities are available begins with a liquid or solid sample, typically 100 to 250 mg, placed in small quartz vial and seated in a sample holder that can be positioned precisely relative to the quartz microprobe or the molecular beam skimmer. The set-up for such a test using a quartz microprobe for sampling is illustrated in Figure 3. The CO<sub>2</sub> laser flux level is set by adjusting the position of a lens relative to the sample, and the flux is measured to ensure that the desired level has been achieved. The desired temporal flux profile is programmed using a PC interface; any flux profile can be programmed. Once the flux is verified and programmed, the test chamber is sealed and flushed with the desired ambient gas. The testing is triggered from a PC and data is collected using Extrel's Merlin data acquisition system. Data reduction is performed using calibration based on actual standards whenever possible, but approximate calibrations are estimated when necessary using a semi-empirical model.<sup>4</sup>

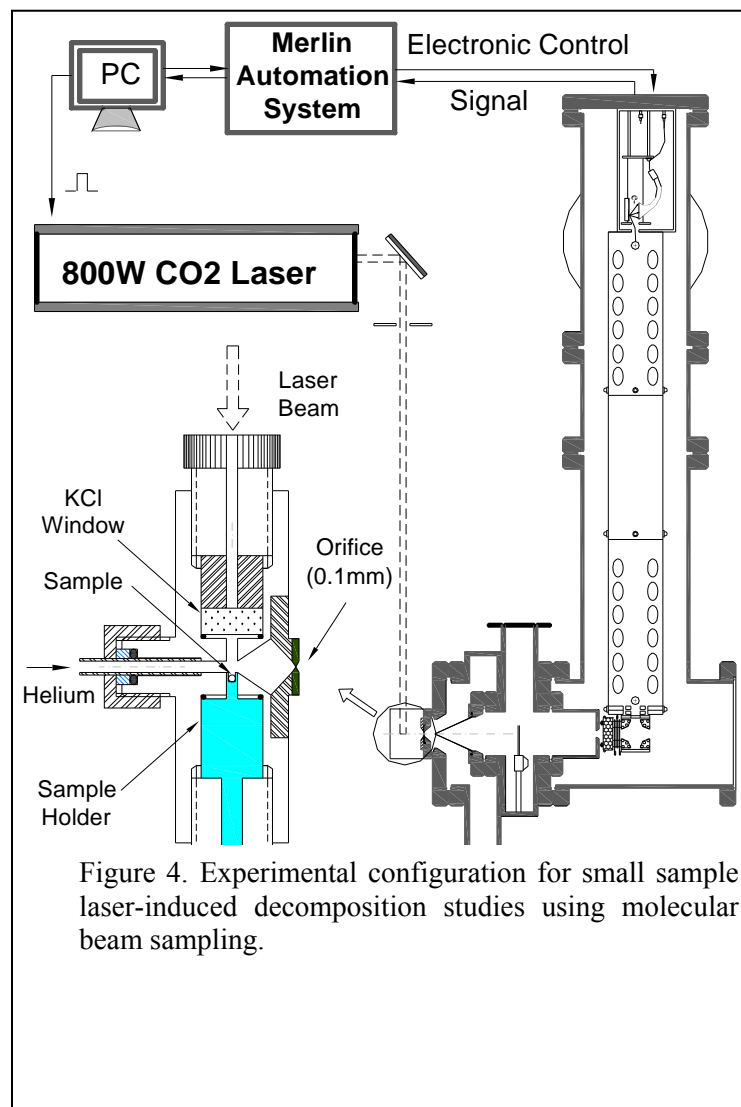


Figure 3. Experimental set-up for mass spectrometer studies showing a burning sample.

Due to the limited quantities of materials available for many of the ionic liquid samples, a new experimental approach was developed for testing milligram level samples. The overall set-up for these experiments is presented in Figure 4. A small sample, on the order of 1 milligram, is placed in the sample pedestal near the molecular beam sampling orifice. The IR-laser enters the test volume through a KCl window and impinges normally on the sample. Just prior to the firing of the laser, a slow flow of helium is started to carry the gas-phase products to the sampling orifice.

To identify species, the capabilities of the TQMS are utilized. Initial experiments are performed to identify the parent ions present in the system. Low electron energies (~22 eV) are used to reduce fragmentation of the parent ions. Once the parents have been identified, additional experiments are performed with MS/MS to determine the fragmentation patterns of the parent ion and to use those patterns to postulate its structure. MS/MS experiments are often done at two different collision energies to assist in the identification of the parent. Given that the test materials contain ions, some molecular beam sampling experiments are always conducted without electron impact to determine if any ions are reaching the gas-

phase. To date, none of these tests have identified ions in the gas-phase, most likely because of the relatively high pressures at which the tests are conducted.





### 3 SUMMARY OF RESULTS

Decomposition reactions were studied for families of methyl-amino-triazolium salts and tetrazolium salts with nitrate anions as well as halide anions. Studies were also conducted with the hypergolic dicyanamide compounds. The following sections summarize the major findings for the triazolium and tetrazolium compounds as well as the hypergolic dicyanamide materials<sup>1</sup>. Detailed discussion of the results of this project can be found in the Ph.D. thesis of Arindrajit Chowdhury, *Confined Rapid Thermolysis/FTIR/ToF Studies of Energetic Ionic Liquids*. Electronic copies of the thesis will be provided upon request to the PI, Thomas Litzinger, at talme@enr.psu.edu.

#### 3.1 Amino-triazolium Compounds

Thermal decomposition of the energetic ionic liquids, 1-methyl-4-amino-1,2,4-triazolium nitrate and 1-amino-3-methyl-1,2,3-triazolium nitrate, was studied by confined rapid thermolysis. Their iodide salts were also studied to provide baseline information on the decomposition of the cation in the absence of a reactive anion. In addition, global kinetic parameters were obtained for the decomposition of 4-amino-1,2,4-triazolium nitrate using inverse analysis; ammonium nitrate was also studied as a reference compound.

Sub-milligram quantities of the compounds were subjected to decomposition under isothermal conditions achieved by initially heating the sample at rates of approximately 2000 K/s. The products formed by decomposition under the afore-mentioned conditions were sampled by rapidscan FTIR spectroscopy and time-of-flight mass spectrometry. Decomposition studies involving the iodide salts were carried out around 270–290°C, whereas the nitrate salts were subjected to 320–340°C. The amino group was found to be involved in the initiation reaction, forming copious quantities of ammonia from the iodide compounds and, N<sub>2</sub>O and H<sub>2</sub>O from the nitrate compounds. The extent of decomposition of the triazole ring was minimal at the test temperatures.

The molecular structures of the molecules are shown in Fig. 5. Studies were also conducted on the building blocks for these molecules, including 4-amino-1,2,4-triazole (4AT), 1-methyl-1,2,4-triazole (1MeTA), and 1-amino-1,2,3-triazole.

---

<sup>1</sup> The research team wishes to acknowledge the EIL team at Edwards and also Jean'ne Shreeve's group for providing many of the materials used in the work on this project.

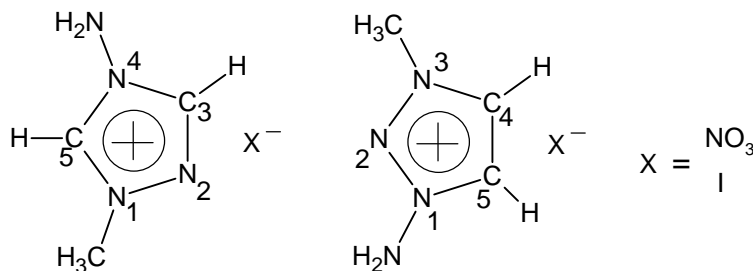


Figure 5: Structure of 1-methyl-4-amino-1,2,4-triazolium X (X = iodide and nitrate) and 1-amino-3-methyl-1,2,3-triazolium X (X = iodide and nitrate).

### 3.1.1 Decomposition pathways of 1-methyl-4-amino-1,2,4-triazolium nitrate

Figure 6a depicts an FTIR spectrum of species from rapid thermolysis of 1-methyl-4-amino-1,2,4-triazolium nitrate at 320°C and 1 atm. Nitric acid ( $\text{HNO}_3$ ), with several rovibrational bands from 1700 to 800  $\text{cm}^{-1}$  and an overtone above 3500  $\text{cm}^{-1}$ , was immediately discernable as a major species. The other major species detected were  $\text{H}_2\text{O}$ ,  $\text{N}_2\text{O}$ , and  $\text{CO}_2$ . Also identified were small quantities of  $\text{HNCO}$  and  $\text{HCN}$ . Figure 6b shows the spectrum obtained by vaporizing 1-methyl-1,2,4-triazole for identification of the bands in the ‘fingerprint region’. It was clear that the decomposition products of 1-methyl-4-amino-1,2,4-triazolium nitrate contained the stable compound 1-methyl-1,2,4-triazole, as evident from the presence of the C–H wags near 850  $\text{cm}^{-1}$ , and the ring torsion near 680  $\text{cm}^{-1}$ . As expected, methyl nitrate ( $\text{CH}_3\text{ONO}_2$ ) was not detected among the products. The findings obtained from FTIR analysis were confirmed by ToF mass spectra.

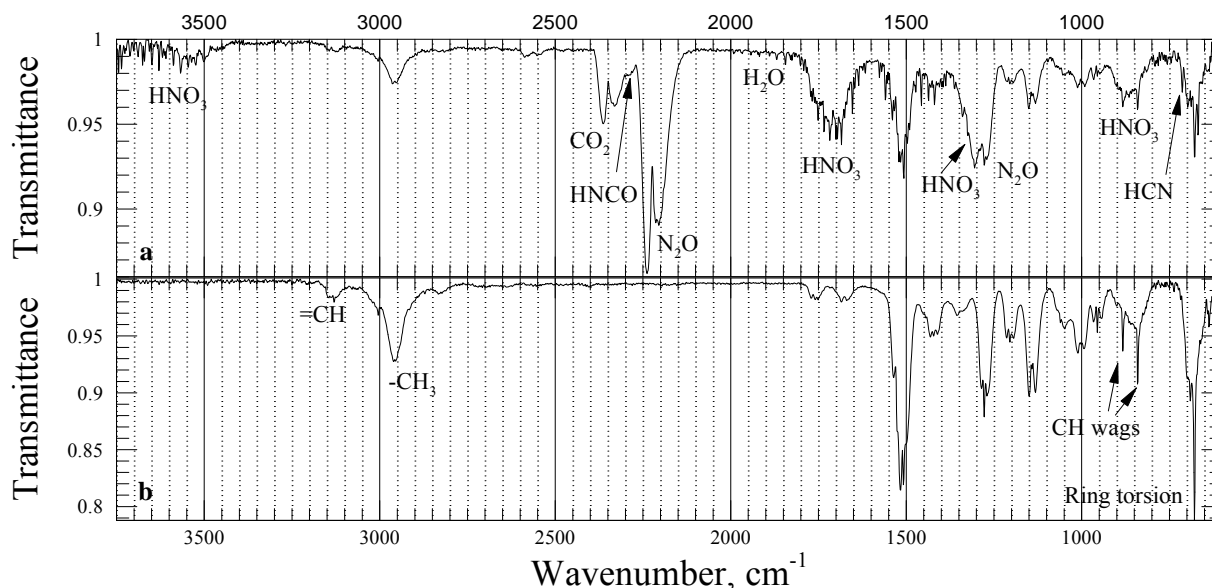


Figure 6: FTIR spectrum of species from rapid thermolysis of (a) 1-methyl-4-amino-1,2,4-triazolium nitrate at 320°C and 1 atm N<sub>2</sub>, and (b) MeTA at 250°C and 1 atm N<sub>2</sub>.

As shown in Fig. 7, the species evolution profiles, extracted from the FTIR spectra acquired at 320°C, reveals further information on the decomposition pathways of 1-methyl-4-amino-1,2,4-triazolium nitrate. Although HNO<sub>3</sub> was found to be a major product during the decomposition of 1-methyl-4-amino-1,2,4-triazolium nitrate, its rate of evolution was significantly delayed compared to the faster rates of H<sub>2</sub>O and N<sub>2</sub>O. CO<sub>2</sub> and HCN were found to evolve at smaller quantities. The right vertical axis shows the absorbance of the band from 1100 to 1175 cm<sup>-1</sup> arising from 1-methyl-1,2,4-triazole. As seen from this plot, 1-methyl-1,2,4-triazole desorbs at a rate comparable to H<sub>2</sub>O and N<sub>2</sub>O from the condensed phase.

The nitrate anion and the complex structure of the amino-methyl-triazole result in a wide variety of reactions leading to the decomposition of 1-methyl-4-amino-1,2,4-triazolium nitrate. However, the formation of H<sub>2</sub>O and N<sub>2</sub>O early in the event, and the lack of methyl nitrate suggest that the initiation reaction involves the amino group. Possible reaction pathways are shown in Fig. 8. The initiation reaction is through an N<sub>4</sub>-N bond scission to form 1-methyl-1,2,4-triazole and the reactive species, NH<sub>2</sub>ONO<sub>2</sub>. NH<sub>2</sub>ONO<sub>2</sub> subsequently forms N<sub>2</sub>O, H<sub>2</sub>O and N<sub>2</sub> through secondary reactions with the parent molecule 1-methyl-4-amino-1,2,4-triazolium nitrate. Methyl-triazolium nitrate, formed as a byproduct during these reactions, decomposes to form the HNO<sub>3</sub> detected at a later stage, and additional 1-methyl-1,2,4-triazole. 1-methyl-1,2,4-triazole produced during the initiation and secondary steps may react with HNO<sub>3</sub> to produce CO<sub>2</sub>, HCN, HNCO, H<sub>2</sub>O and N<sub>2</sub>.

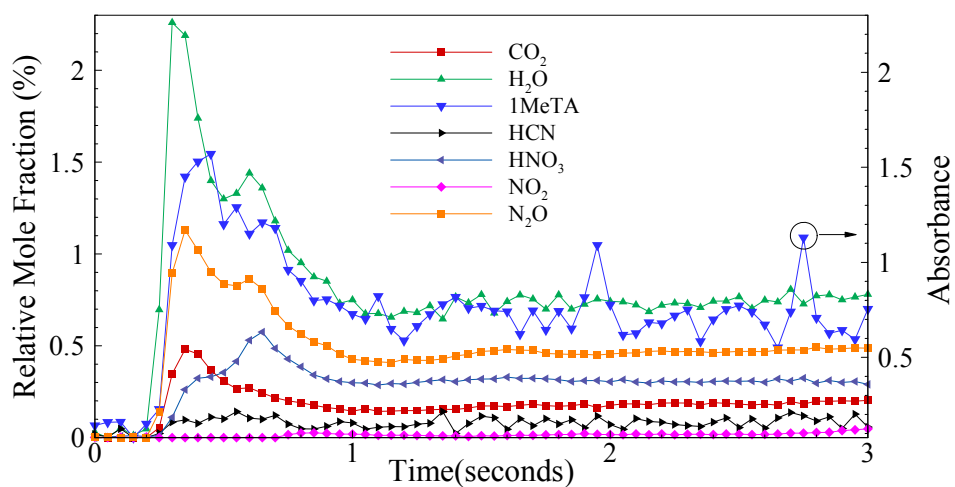


Figure 7: Species evolution from rapid thermolysis of 1-methyl-4-amino-1,2,4-triazolium nitrate at 320°C and 1 atm N<sub>2</sub>.

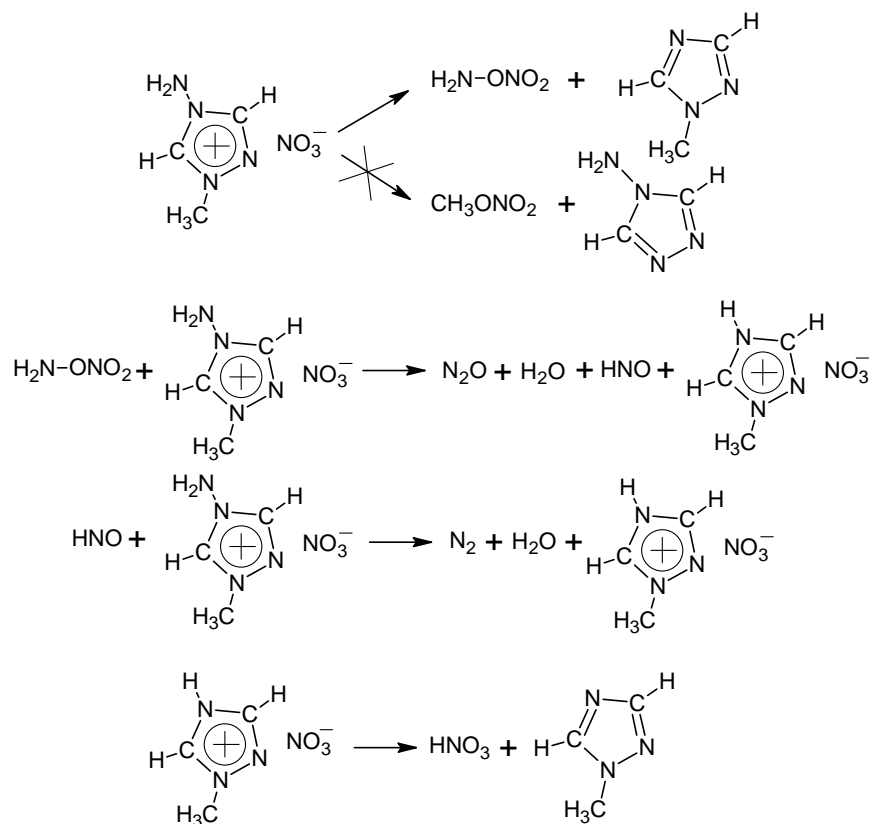


Figure 8. Proposed reaction scheme for 1-methyl-4-amino-1,2,4-triazolium nitrate

### 3.1.2 Decomposition pathways of 1-amino-3-methyl-1,2,3-triazolium nitrate

Figure 9 shows an FTIR spectrum of the gaseous products generated during thermolysis of 1-amino-3-methyl-1,2,3-triazolium nitrate at 340°C and 1 atm. The major species present among the decomposition products were HNO<sub>3</sub>, H<sub>2</sub>O and N<sub>2</sub>O, similar to the FTIR spectra obtained from 1-methyl-4-amino-1,2,4-triazolium nitrate. Besides these principal species, smaller quantities of CO<sub>2</sub>, NO<sub>2</sub>, and HNCO were also detected. Though it was difficult to exactly ascertain the presence of 3-methyl-1,2,3-triazole, the band due to ring torsion around 760 cm<sup>-1</sup> and the -CH<sub>3</sub> stretch near 3000 cm<sup>-1</sup> indicate its formation. Due to overlapping of bands, it was not possible to exactly identify CH<sub>3</sub>ONO<sub>2</sub>, if present, among the products.

Figure 10 shows a ToFMS spectrum from the thermolysis of 1-amino-3-methyl-1,2,3-triazolium nitrate taken at 340°C and 1 atm Ar, He and residual air. Similar to 1-methyl-4-amino-1,2,4-triazolium nitrate, the decomposition products include HNO<sub>3</sub>, as seen from the peaks at m/z = 46 and m/z = 30. The peaks at m/z = 83 and m/z = 84 shows the presence of 3-methyl-1,2,3-triazole and its protonated form. The smaller species found in the FTIR spectra, such as H<sub>2</sub>O at m/z = 18, N<sub>2</sub>O and CO<sub>2</sub> at m/z = 44 are also present. The fragmentation of 3-methyl-1,2,3-triazole leads to the smaller peaks at m/z = 55, 54, 52, 42, and 27.

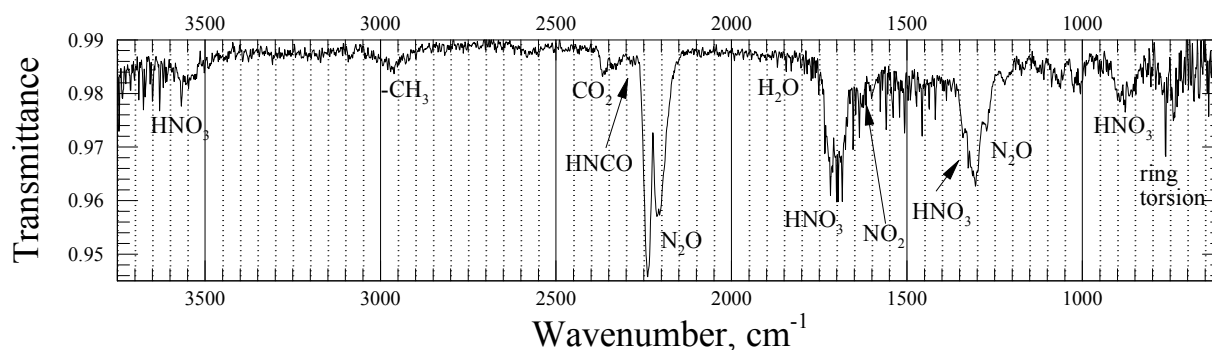


Figure 9: FTIR spectrum of species from rapid thermolysis of 1-amino-3-methyl-1,2,3-triazolium nitrate at 340°C and 1 atm N<sub>2</sub>.

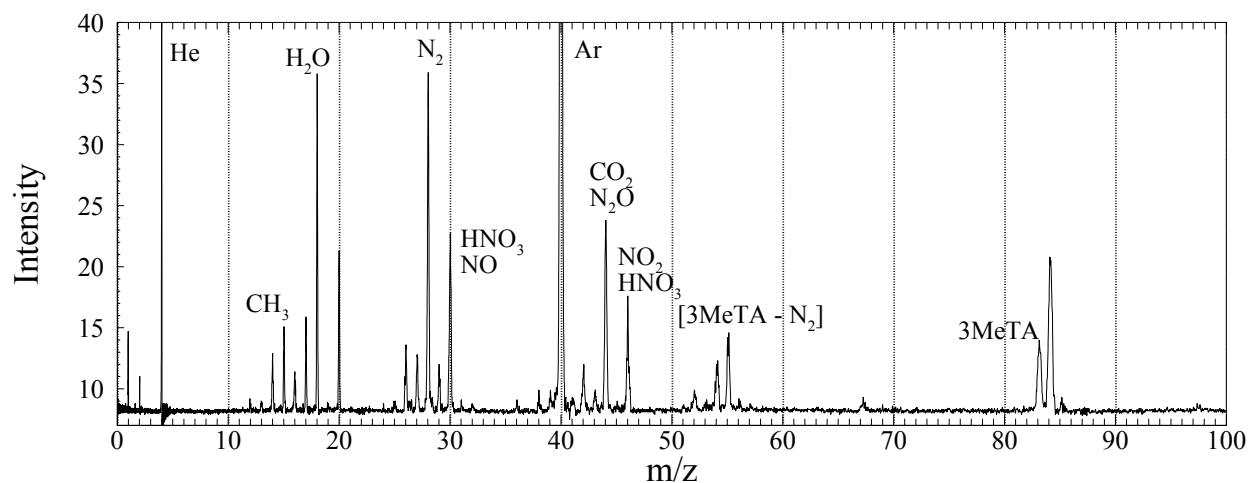


Figure 10: Mass spectrum from rapid thermolysis of 1-amino-3-methyl-1,2,3-triazolium nitrate at 340°C and 1 atm Ar, He and residual air (average of 10 spectra).

In order to further elucidate the decomposition pathways of 1-amino-3-methyl-1,2,3-triazolium nitrate, the species evolution profiles were extracted from the FTIR spectra at 340°C and displayed in Fig. 11. The pattern of evolution of various species was found to be remarkably similar to 1-methyl-4-amino-1,2,4-triazolium nitrate, with H<sub>2</sub>O and N<sub>2</sub>O desorbing from the condensed phase at a fast rate, followed by HNO<sub>3</sub>. As observed in case of 1-methyl-4-amino-1,2,4-triazolium nitrate, the evolution of HNO<sub>3</sub> is considerably delayed.

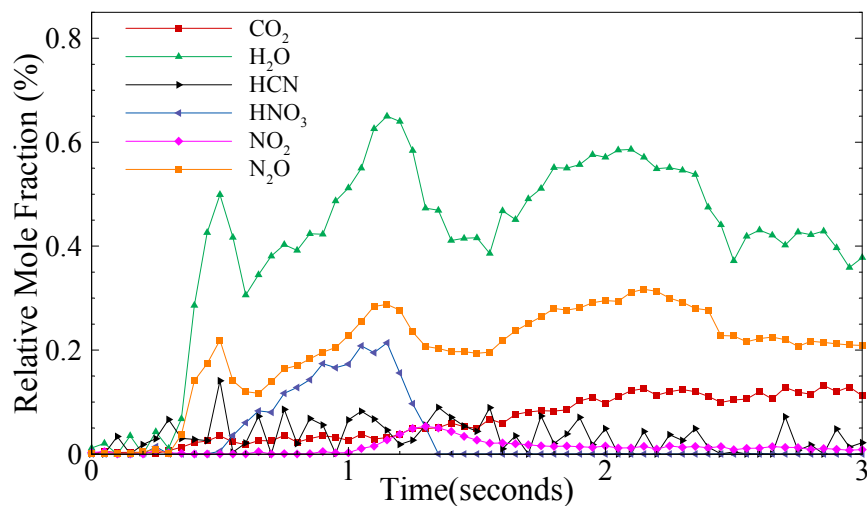


Figure 11: Species evolution from rapid thermolysis of 1-amino-3-methyl-1,2,3-triazolium nitrate at 340°C and 1 atm N<sub>2</sub>.

Based on the FTIR and ToFMS spectra, and the knowledge gained from studying the decomposition of iodide salt and 1-methyl-4-amino-1,2,4-triazolium nitrate, possible decomposition pathways of 1-amino-3-methyl-1,2,3-triazolium nitrate are shown in Figure 11. The decomposition of 1-amino-3-methyl-1,2,3-triazolium nitrate was mostly similar to that of 1-methyl-4-amino-1,2,4-triazolium nitrate. The primary reaction pathway involves the formation of  $\text{NH}_2\text{ONO}_2$  and 3-methyl-1,2,3-triazole. The smaller species  $\text{N}_2\text{O}$  and  $\text{H}_2\text{O}$  are formed via fast secondary reactions. Methyl-triazolium nitrate, formed as a byproduct during these reactions, decomposes to form the  $\text{HNO}_3$  detected at a later stage, and more 3-methyl-1,2,3-triazole. Additionally, 3-methyl-1,2,3-triazole was oxidized by nitric acid to form the smaller molecular weight species.

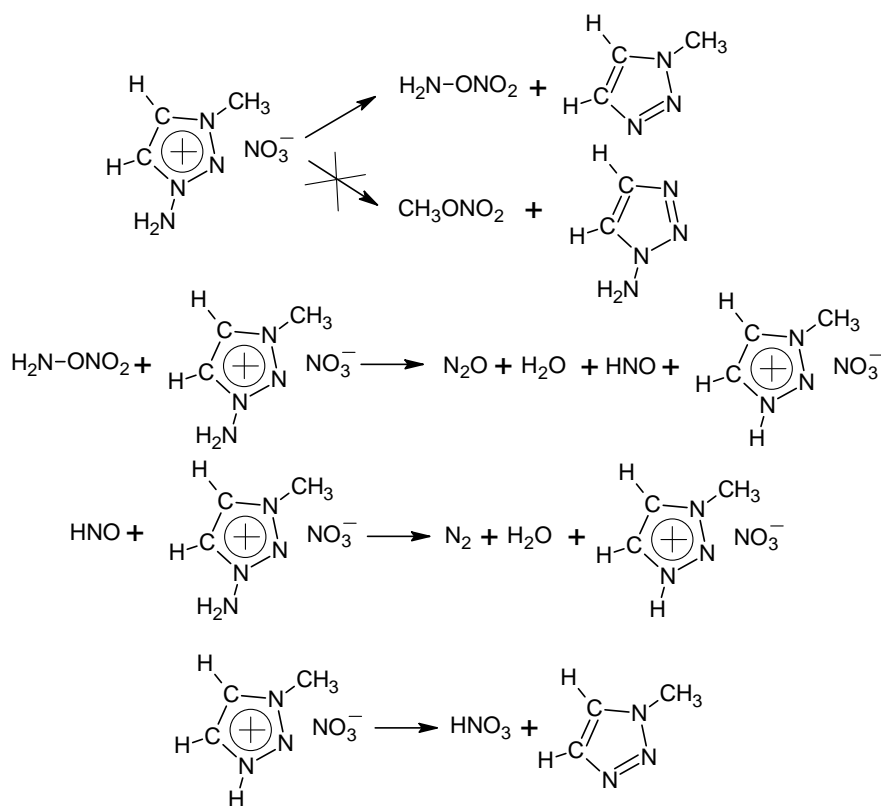


Figure 11. Proposed reaction scheme for 1-amino-3-methyl-1,2,3-triazolium nitrate

### 3.1.3 Global decomposition kinetics of 4-amino-1,2,4-triazolium nitrate

The Arrhenius-type reaction rate parameters for the initiation reactions governing the thermal decomposition of 4-amino-1,2,4-triazolium nitrate (4ATN) were determined by numerical techniques. The supplementary compounds studied for comparison were 4-amino-1,2,4-triazolium chloride (4ATCl) and ammonium nitrate (AN). The reaction rate parameters were obtained by an evolutionary genetic algorithm that compared the difference between the experimental and simulated species evolution profiles from the decomposition process. The experimental data were generated by confined rapid thermolysis. The decomposition process was simulated by applying conservation equations to the condensed and gas phases individually. The optimization module recovered the experimental species profiles with reasonable accuracy for all the compounds studied. The processes governing the decomposition of these energetic compounds were found to be autocatalytic in nature, and the autocatalytic agents were the strong acids generated by the initial decomposition step. The activation energy and pre-exponential factor for the unimolecular decomposition step for 4-amino-1,2,4-triazolium nitrate and 4ATCl were 40–45 kcal/mol and  $10^{16}$ , respectively, similar to previously determined values for AN by Rubstov et al.<sup>5</sup>

Species profiles observed during thermolysis of 0.466 mg of 4-amino-1,2,4-triazolium nitrate under 290°C and one atm pressure are shown in Fig. 12.  $\text{HNO}_3$  is the first species to desorb from the condensed phase, followed by  $\text{H}_2\text{O}$  and  $\text{N}_2\text{O}$  at slower rates.  $\text{CO}_2$  and smaller quantities of HCN were also detected among the secondary reaction products. Contrary to the cases of AN and 4ATCl,  $\text{NH}_3$  is not detected in the gas-phase, so it would appear that it reacts in the condensed phase. The 1,2,4-triazole produced during the decomposition process attacks the  $\text{HNO}_3$ , forming triazolium nitrate in the process, and leading to the subsequent disappearance of  $\text{HNO}_3$ , and setting the temporal bound for the kinetic study at 750 ms. The onset of decomposition occurs through a proton scavenging by the nitrate ion from the amino group on the 4-amino-triazolium cation, forming  $\text{HNO}_3$  and the remaining species, named 4ATz, which is a combination of 1,2,4-triazole and the imino radical.



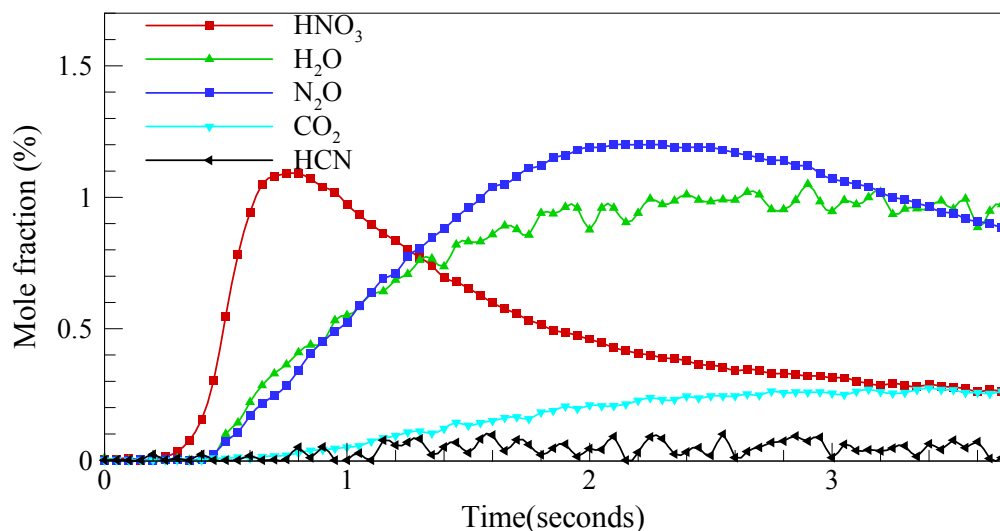


Figure 12: Species evolution from rapid thermolysis of 0.466 mg of 4-amino-1,2,4-triazolium nitrate at 290°C and 1 atm N<sub>2</sub>.

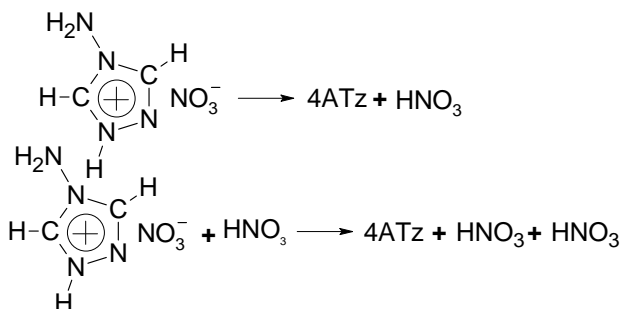


Figure 13: Proposed reaction scheme for 4-amino-1,2,4-triazolium nitrate

Two initiation reactions presented in Fig. 13 were considered for the reaction of 4-amino-1,2,4-triazolium nitrate. The parameter regimes explored for the uni-molecular decomposition step were 30–50 kcal/mol and  $10^{12}$ – $10^{20}$  s<sup>-1</sup> for the activation energy and the pre-exponential factor, respectively. Attempts to determine overall reaction parameters using only the first reaction in Fig. 13 led to unrealistically large values of the pre-exponential factor, even though the experimental species evolution profiles were adequately recovered. The incorporation of the autocatalytic step in the reaction mechanism shown in scheme I led to the best-fit reaction parameters given in Table 1.

Table 1: Estimated Global Arrhenius-type parameters of decomposition.

Reaction Mechanism	Activation energy (kcal/mol)	Preexponential Factor <sup>a</sup>
$\text{NH}_4\text{NO}_3 \rightarrow \text{NH}_3 + \text{HNO}_3$	45	$3.9 \times 10^{15}$
$\text{NH}_4\text{NO}_3 + \text{HNO}_3 \rightarrow \text{NH}_3 + \text{HNO}_3 + \text{HNO}_3$	21	$3.5 \times 10^{10}$
$4\text{ATCl} \rightarrow 4\text{AT} + \text{HCl}$	43	$7.9 \times 10^{16}$
$4\text{ATCl} + \text{HCl} \rightarrow 4\text{AT} + \text{HCl} + \text{HCl}$	23	$1.5 \times 10^{12}$
$4\text{ATN} \rightarrow 4\text{ATz} + \text{HNO}_3$	42	$1.4 \times 10^{16}$
$4\text{ATN} + \text{HNO}_3 \rightarrow 4\text{ATz} + \text{HNO}_3 + \text{HNO}_3$	29	$5.7 \times 10^{13}$

<sup>a</sup>Units are s, cm<sup>3</sup>, mol

Values for the two reaction steps of AN are reported in the literature by Rubstov et al.<sup>5</sup> They are: 47.2 kcal/mol and  $2.5 \times 10^{14} \text{ s}^{-1}$  for the first step, and 24.0 kcal/mol and  $2 \times 10^7 (\text{mol/cc} \times \text{s})^{-1}$  for the second step. Except for the pre-exponential factor for the autocatalytic step, the other parameters for AN are in fair agreement with the literature. The large difference in the pre-exponential factor for the autocatalytic step may be due to differences in experimental conditions, in particular reaction temperatures, which were higher by approximately 100°C in the present experiments, leading to faster vaporization and thus, less accumulation of HNO<sub>3</sub>, the autocatalytic agent.

### 3.2 Tetrazolium salts

The tetrazolium compounds (Fig. 14) studied were 2-amino-4,5-dimethyl-tetrazolium nitrate and 1-amino-4,5-dimethyl-tetrazolium nitrate along with iodide analogs. 2-amino-4,5-dimethyl-tetrazolium nitrate was studied at temperatures of approximately 300°C. 1-amino-4,5-dimethyl-tetrazolium nitrate was found to be more reactive, therefore, it was studied at temperatures approximately 50°C lower.

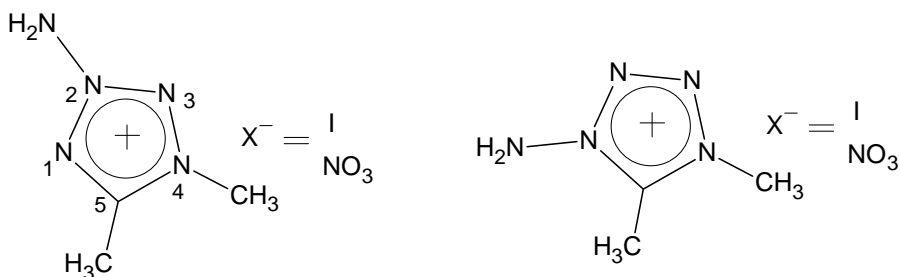


Figure 14: Structures of 2-amino-4,5-dimethyl-tetrazolium X (X = iodide and nitrate), and 1-amino-4,5-dimethyl-tetrazolium X (X = iodide and nitrate).

#### 3.2.1 Decomposition pathways of 2-amino-4,5-dimethyl-tetrazolium nitrate (2-AdMTZN)

2AdMTZN is a white crystalline solid with a melting point of 94°C, considerably lower than the corresponding iodide salt. The hygroscopic nature of the salt made it difficult to study the decomposition behavior of the compound. The sample was dried for 24 hours under vacuum (40 mtorr) and then stored in a sealed container to avoid contamination by moisture. Small quantities of the sample were thermolysed at temperatures near 300°C, with a sooty black residue left on the aluminum foil. Figure 15 shows an FTIR spectrum of the gaseous products generated during the thermolysis of 2AdMTZN at 300°C and 1 atm. Methyl nitrate (CH<sub>3</sub>ONO<sub>2</sub>), with several rovibrational bands from 1700 to 800 cm<sup>-1</sup> was immediately discernable as the principal species. Also detected were H<sub>2</sub>O, CO<sub>2</sub>, and a small quantity of HCN. The common oxides of nitrogen, NO, N<sub>2</sub>O, and NO<sub>2</sub> were surprisingly absent in Fig. 15. The double bands around 2260 cm<sup>-1</sup> and 2310 cm<sup>-1</sup> were identified as a combination of methyl isocyanate (CH<sub>3</sub>NCO) and CH<sub>3</sub>CNO, respectively. Around 1750 cm<sup>-1</sup>, a strong band due to a species containing a C=O bond was detected. Aldehydes and ketones normally show strong features in the range from 1,700 to 1,750 cm<sup>-1</sup>. As found in the FTIR spectra of 2AdMTZI, CH<sub>3</sub>NC was present with a band at 2160 cm<sup>-1</sup>.

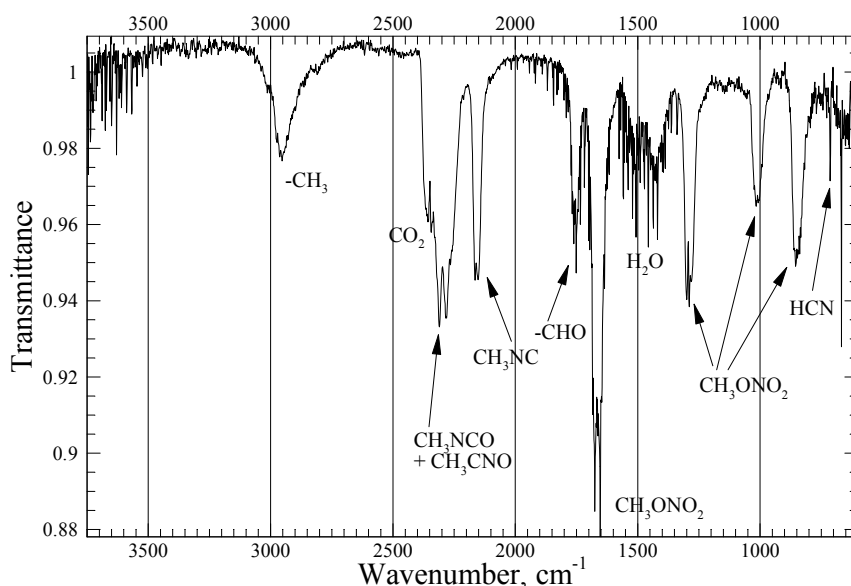


Figure 15: FTIR spectrum of species from rapid thermolysis of 2AdMTZN at 300°C and 1 atm N<sub>2</sub>.

Figure 16 shows a spectrum from the ToFMS acquired during the pyrolysis of 2AdMTZN at 300°C and 1 atm Ar, He and residual air extracted 0.12s after the two heaters came into contact. Although CH<sub>3</sub>ONO<sub>2</sub> is absent from the mass spectrum at a cursory glance, its presence was confirmed by prominent peaks of CH<sub>3</sub><sup>+</sup> (*m/z*=15), NO<sub>2</sub><sup>+</sup> (*m/z*=46), and NO<sup>+</sup> (*m/z*=30), corroborated by Fischer et al.<sup>6</sup> during thermal decomposition of 1,5-diamino-4-methyl-tetrazolium nitrate. The peak at *m/z* = 99 was confirmed as an amino-methyl-tetrazole, and after a brief study of the fragments, was identified as 2A5MeTZ. The smaller molecular-weight species of N<sub>2</sub> and H<sub>2</sub>O were also present in Fig. 16. The larger peak at *m/z* = 57, in comparison to the mass spectra obtained during thermolysis of 2AdMTZI indicates that other species are present besides the fragments of 2A5MeTZ. The FTIR spectra confirm that these species are indeed CH<sub>3</sub>NCO and CH<sub>3</sub>CNO. The aldehyde present in the FTIR spectrum was recognized as acetaldehyde (*m/z* = 44) after deliberation.

The presence of the energetic nitrate anion and the complex structure of the tetrazole complicate the reactions leading to the decomposition of 2AdMTZN. However, the apparent abundance of CH<sub>3</sub>ONO<sub>2</sub> and 2A5MeTZ indicates the presence of possible reaction involving the methyl group. Possible major pathways for decomposition are summarized in Table 2. *Ab initio* calculations at the B3LYP/6-31++G\*\* level corroborate that the major reaction channel remains unaltered from the one observed for 2AdMTZI. The affinity of the nitrate group for the methyl group over the amino group has also been established while studying decomposition behavior of 1,5-diamino-4-methyl-1*H*-tetrazolium nitrate.

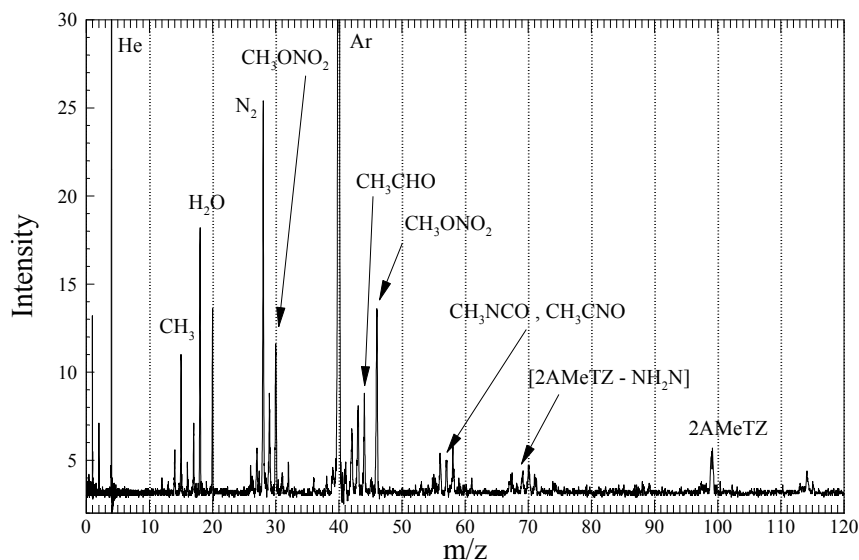
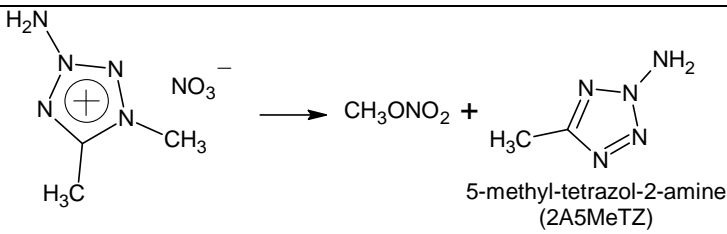
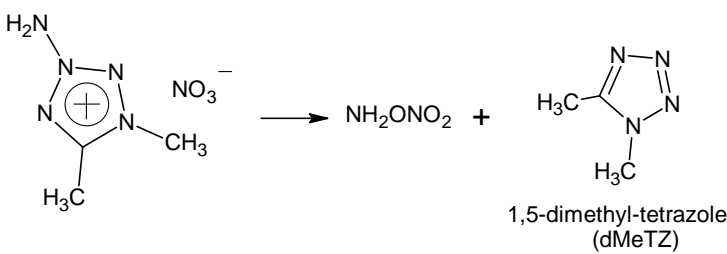
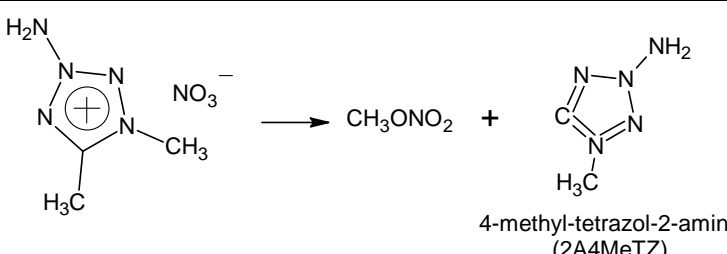


Figure 16: Mass spectrum from rapid thermolysis of 2AdMTZN at 300°C and 1 atm Ar, He and residual air extracted at 0.12s (average of 10 spectra).

The possible secondary reactions between the products formed are outlined in Figure 17. Possible condensed-phase reactions between  $\text{CH}_3\text{ONO}_2$  and 2A5MeTZ replace the methyl group on 2A5MeTZ to form 2-amino-5-methoxy-2*H*-tetrazole, detected by a minor peak at  $m/z = 115$  in Fig. 16, and methyl nitrite,  $\text{CH}_3\text{ONO}$ . Similar substitution reactions were observed during the thermolysis of di-alkyl-substituted imidazolium nitrates.<sup>7</sup> The methoxy tetrazole undergoes a decomposition process similar to 2A5MeTZ to form the species  $\text{CH}_3\text{NCO}$  and  $\text{CH}_3\text{CNO}$  through nitrogen elimination. Besides,  $\text{CH}_3\text{ONO}_2$  and  $\text{CH}_3\text{ONO}$  partially decompose under the temperatures applied to form smaller molecules.

Table 2: Theoretical reaction enthalpies and free energies for 2AdMTZN at B3LYP/6-31++G\*\* level.

Reactions		$\Delta H_R$ (kcal/mol)	$\Delta G_R$ (kcal/mol)
1.	 <p>5-methyl-tetrazol-2-amine (2A5MeTZ)</p>	-3.42	-16.24
2.	 <p>1,5-dimethyl-tetrazole (dMeTZ)</p>	5.07	-6.68
3.	 <p>4-methyl-tetrazol-2-amine (2A4MeTZ)</p>	42.78	31.64

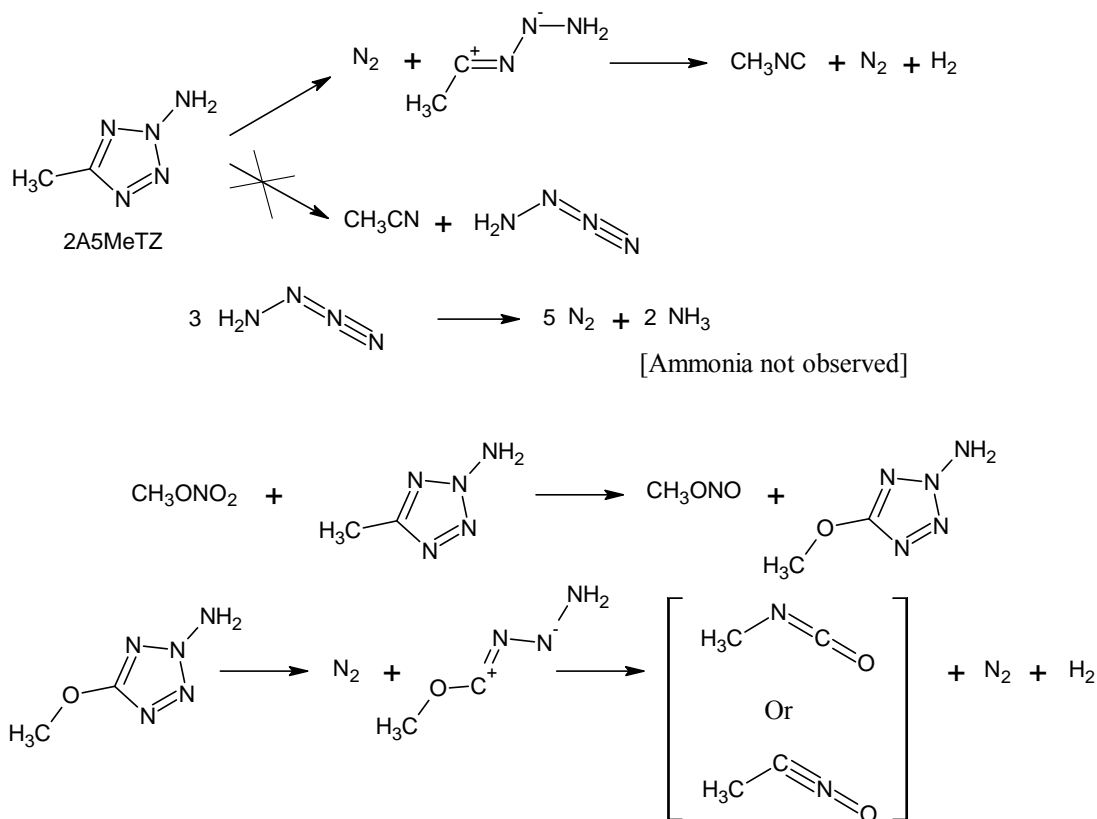


Figure 17: Proposed secondary reaction pathways for 2-amino-4,5-dimethyl-tetrazolium nitrate

### 3.2.2 Decomposition reactions of 1-amino-4,5-dimethyl-tetrazolium nitrate (1AdMTZN)

Confined rapid thermolysis on approximately 0.5  $\mu$ L of the sample was carried out at temperatures around 250°C. The spectrum from these tests was dominated by the rotational structures of  $H_2O$ , centered at 1595  $cm^{-1}$ , making it difficult to ascertain the rovibrational bands present in the region 1200 to 2000  $cm^{-1}$ . In order to determine the species present with water, the concentration of  $H_2O$  was calculated using a data reduction procedure and the amount of  $H_2O$  present was synthetically subtracted to yield the cleaner spectrum shown in Fig. 18. Consequently, the species that were identified are  $CH_3ONO_2$ ,  $NO$ ,  $NO_2$ ,  $N_2O$ ,  $CH_3CNO$ , and  $CH_3NCO$ . Also detected in smaller quantities were  $CO$ ,  $CO_2$ ,  $CH_4$ , and  $CH_3OH$ .

Although  $HCN$  was not detected among the decomposition products of iodide salt, its strong Q-branch at 712  $cm^{-1}$  is clearly present in the spectrum in Figure 18. On the other hand, the large quantities of  $NH_3$  found in the FTIR spectra of iodide salt are not present here, indicating that it has reacted, perhaps with the methyl nitrate formed during the initiation step. An aldehyde was identified by the prominent band near 1750  $cm^{-1}$ . Additionally, the  $N\equiv C$  stretch from the isonitrile,  $CH_3NC$  was found at 2160  $cm^{-1}$ .

ToFMS data taken at 0.09 seconds after initiation of heating clearly show the presence of nitrogen and HCN.

Based on the FTIR and ToFMS data, and the knowledge gained from studying the decomposition of iodide salt, the primary reaction pathways and their associated free energy changes calculated at the B3LYP/6-31++G\*\* level were formulated, as summarized in Table 3. Three major pathways – a nucleophilic transfer involving the methyl group attached to the ring nitrogen to form 1A5MeTZ and  $\text{CH}_3\text{ONO}_2$  (reaction 1), ammonia formation by the amino group through a proton abstraction from the neighboring methyl group (reaction 2), as well as ring nitrogen elimination (reaction 3), were all found to be thermodynamically feasible processes.

Possible secondary reactions leading to the detected species has been given in Figure 19. 1A5MeTZ dissociates with an  $\text{N}_2$  ejection to form mainly ammonia. Unlike the decomposition of 2AdMTZN, where most of the generated  $\text{CH}_3\text{ONO}_2$  desorbed into the gas phase, majority of the nitrate from 1AdMTZN oxidizes  $\text{NH}_3$  to liberate a number of smaller molecular weight species, namely  $\text{N}_2\text{O}$  and  $\text{H}_2\text{O}$ , as well as  $\text{CO}$ ,  $\text{NO}$ ,  $\text{CO}_2$ , and  $\text{NO}_2$ . A portion of  $\text{CH}_3\text{ONO}_2$  reacts through the formation of 1-amino-5-methoxy-1*H*-tetrazole to form  $\text{CH}_3\text{NCO}$  and  $\text{CH}_3\text{CNO}$ , forming  $\text{CH}_3\text{ONO}$  in the process. Besides these primary reactions, numerous other secondary reactions involving the intermediate nitrenes,  $\text{CH}_3\text{ONO}_2$ , and  $\text{CH}_3\text{ONO}$  also take place to form the smaller molecular weight gases.

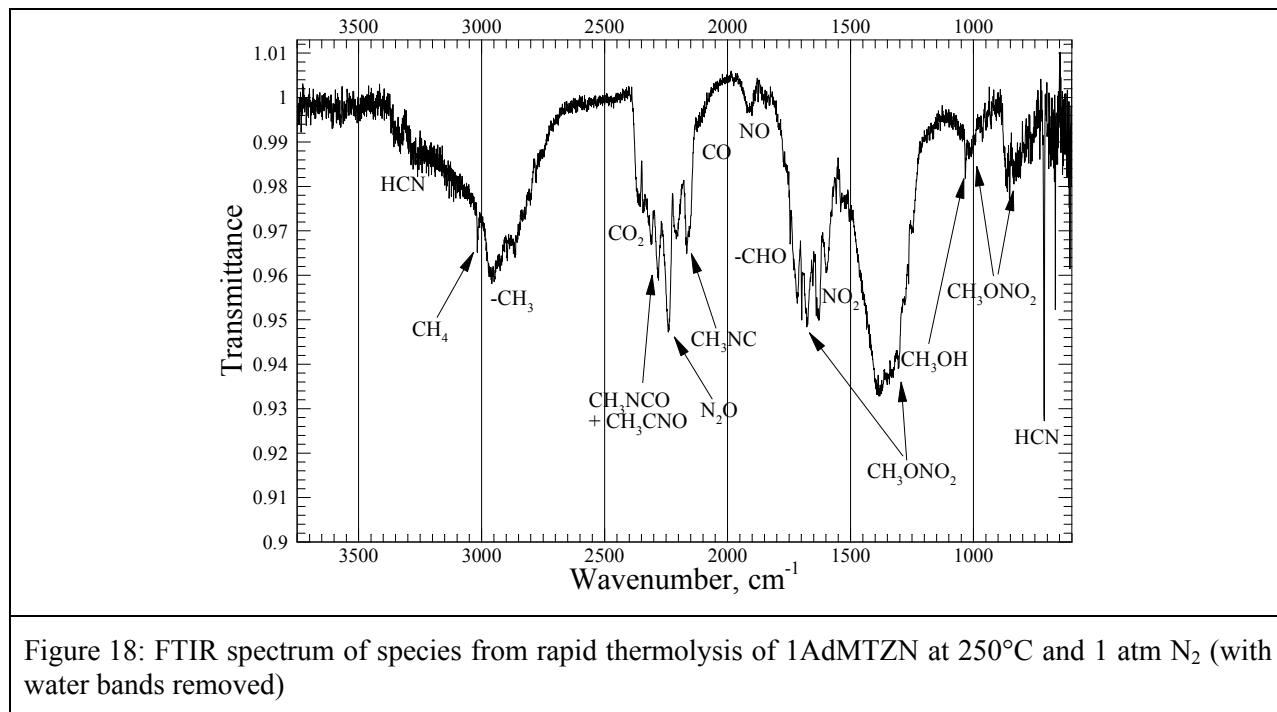
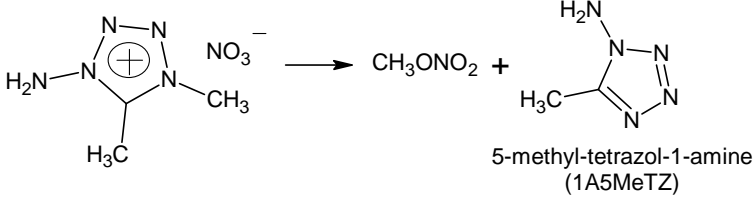
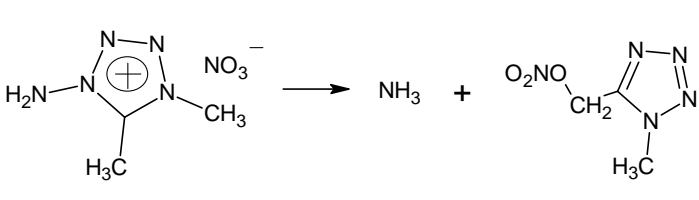
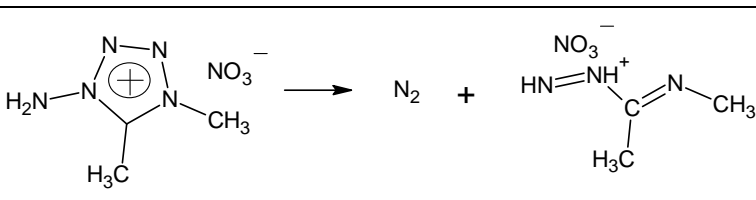
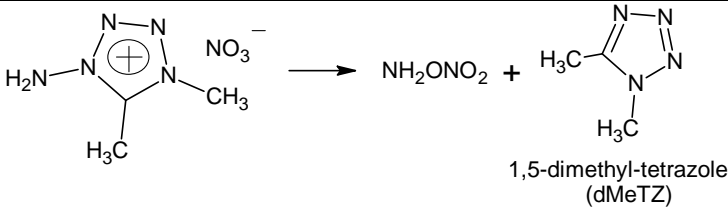
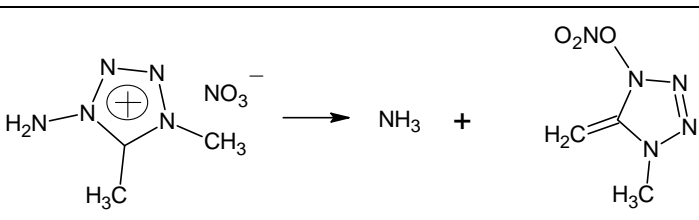
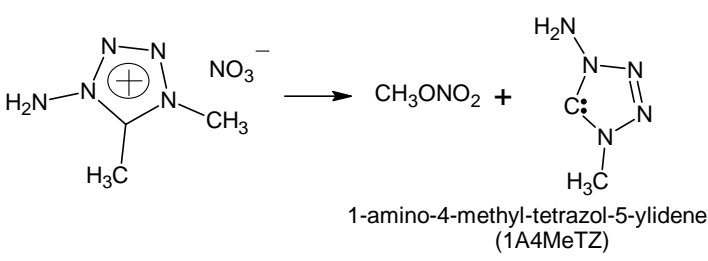
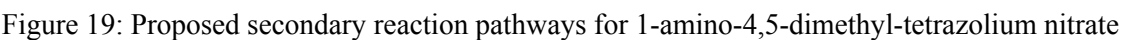


Figure 18: FTIR spectrum of species from rapid thermolysis of 1AdMTZN at 250°C and 1 atm  $\text{N}_2$  (with water bands removed)



Table 3: Theoretical reaction enthalpies and free energies for 1AdMTZN at B3LYP/6-31++G\*\* level.

Reactions	$\Delta H_R$ (kcal/mol)	$\Delta G_R$ (kcal/mol)
<p>1.</p>  <p>5-methyl-tetrazol-1-amine (1A5MeTZ)</p>	0.98	-10.68
<p>2.</p> 	-15.86	-25.9
<p>3.</p> 	-16.24	-28.13
<p>4.</p>  <p>1,5-dimethyl-tetrazole (dMeTZ)</p>	8.64	-3.31
<p>5.</p> 	32.19	21.72
<p>6.</p>  <p>1-amino-4-methyl-tetrazol-5-ylidene (1A4MeTZ)</p>	31.18	19.4



### 3.3 Hypergolic reaction of Dicyanamide Ionic Liquids

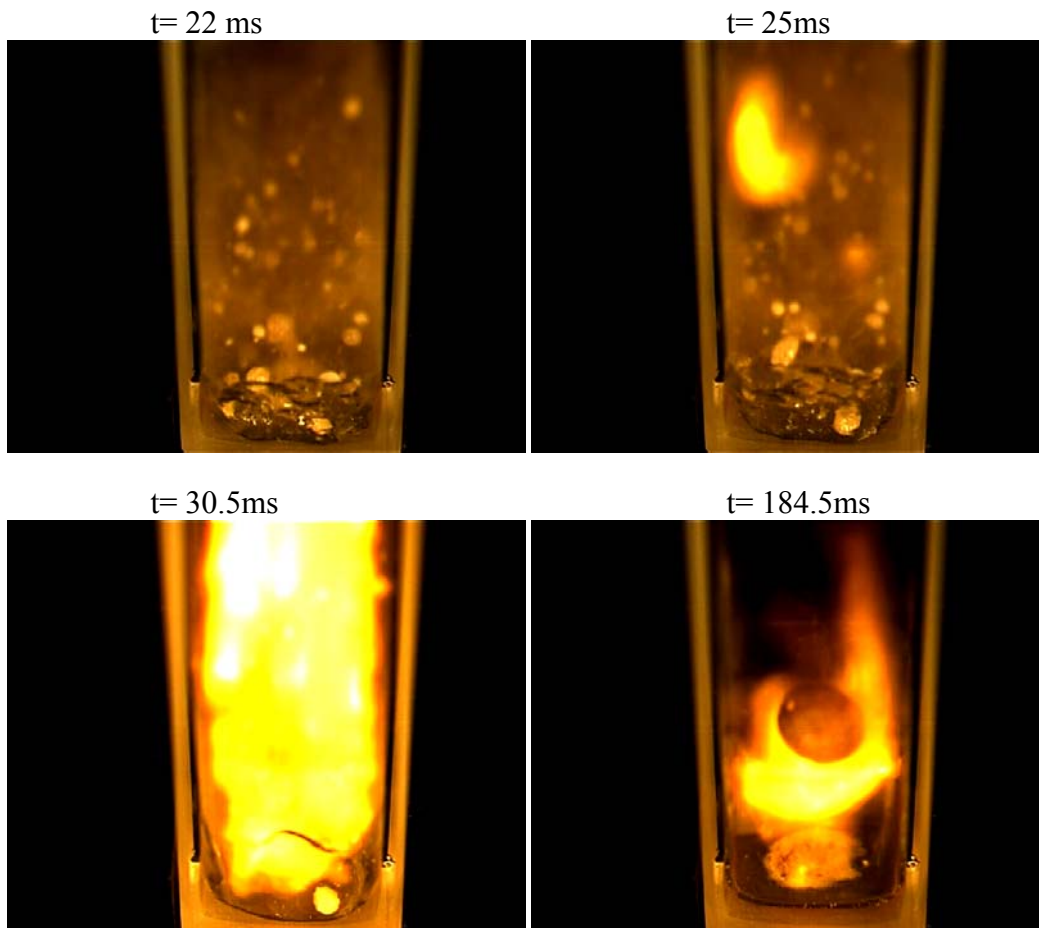
Drop test studies were conducted to observe the reaction at high speed and also to measure the gas-phase reaction temperatures for 1-ethyl-3-methylimidazolium dicyanamide (emimDCA), and 1-butyl-3-methylimidazolium dicyanamide (bmimDCA). In addition detailed reaction studies were performed to verify the mechanism proposed by the Edwards EIL group<sup>8</sup>.

#### 3.3.1 *High speed imaging and temperature measurements*

In the drop tests, the vial was filled with white-fuming nitric acid and the ionic liquid was dropped. A section of the cuvette is removed beforehand to facilitate the placement of the thermocouples necessary for the measurement of temperature. Fine-gage K-type thermocouples, 0.002 inches in diameter, are mounted on individual Teflon plates stacked vertically. The plates are recessed in order to position the cuvette accurately below a syringe containing approximately 10  $\mu$ l of fuel. Special care is taken to align the syringe above the thermocouple assembly to ensure the drop of fuel avoids the thermocouple wires while traveling towards the oxidizer pool.

Table 4 provide selected frames from the high speed movie of the drop test showing the ignition event for 1-ethyl, 3-methylimidazolium nitrate. After a time period during which reaction products and liquid droplets accumulate in the gas phase above the reaction zone, the ignition kernel is formed at about 25 ms after the droplet impact. The kernel expands to a luminous flame within a short period of time, traveling downwards as well as upwards towards the open end of the cuvette, filling the cuvette with luminosity. The combustion process is short-lived owing to constraints on the amount of fuel introduced into the system. Copious amounts of charred material are formed in the process and are deposited along the walls of the cuvette.

Table 4: Selected frames acquired during ignition occurring after impingement of an EmimDCA droplet on WFNA.



Besides the high speed videos of the hypergolic ignition event, temperature profiles at three locations in the gas phase were also acquired to provide further insight into the gas phase phenomena. Figure 20 shows the variation of temperature in the ignition zone, coupled with a photodiode trace monitoring the visible emission during ignition, as a  $10 \mu\text{l}$  drop of EmimDCA impinged upon  $160 \mu\text{l}$  of  $90\% \text{HNO}_3$ . The thermocouples were numbered one to three, in order of increasing distance from the oxidizer surface. As evident from the plot, no temperature rise is detected for approximately 35 ms after the droplet impact. This period, as corroborated by the high speed images, is dominated by mixing between the two reactants, and subsequent condensed phase reactions along the mixing interface. After this initial phase, the gaseous products as well the condensed phase globules enter the gas phase. These elements combined with the heat feedback from the exothermic liquid phase reactions cause a sharp inflection point in the temperature

profile recorded by the first thermocouple. The arrival of this point is delayed for the subsequent thermocouples due to the temporal lag introduced by the gas transport across the half-inch distance between consecutive thermocouples.

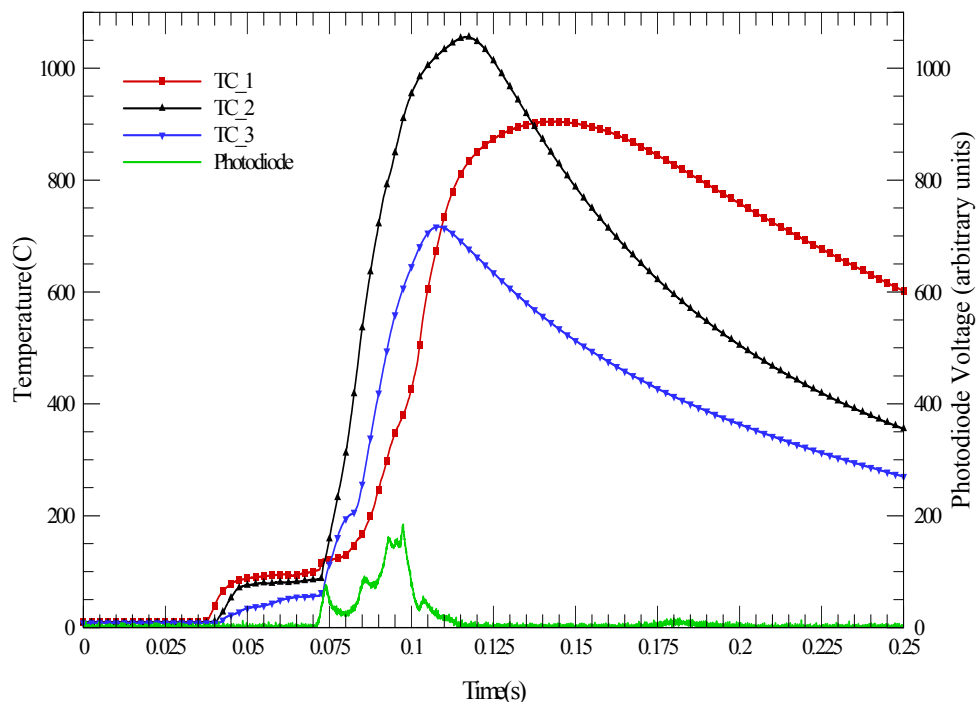


Figure 20: Temperature profiles and photodiode output from hypergolic reaction of an impinging EmimDCA droplet on 90%  $\text{HNO}_3$ .

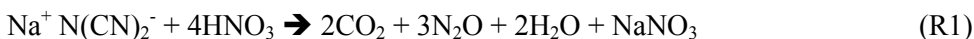
After the initial rise in temperatures, the temperature at the first and the second thermocouples remain constant at approximately  $100^\circ\text{C}$  and  $90^\circ\text{C}$  for 35 ms, signaling an accumulation of gaseous species in the ignition zone. However, the thermocouple farthest from the reaction zone records a gradual rise in temperatures up to  $60^\circ\text{C}$ . At the end of this period, which may be termed as an induction period, the ignition kernel is formed in the gas phase, and introduces the second inflection point in the temperature profiles. The ignition point was also clearly identifiable from the sharp rise in the photodiode signal. The global ignition delay for a system comprising of  $10\ \mu\text{l}$  of EmimDCA and  $160\ \mu\text{l}$  of 90%  $\text{HNO}_3$  was thus determined to be 70 ms. After the initiation of combustion, the temperatures of the first, second and the third thermocouples rose sharply to attain their maximum values of  $900^\circ\text{C}$ ,  $1050^\circ\text{C}$  and  $720^\circ\text{C}$ , respectively. The temperature profiles gradually declined after the combustion event was over, as identified by the return of the photodiode signal to its base level. The presence of several peaks in the photodiode signal was consistent with the videos taken of the event with the high speed camera, where the flame front was found to grow and diminish over the duration of the combustion event.

### 3.3.2 Investigations of hypergolic ignition chemistry in drop tests

In this set of experiments sodium dicyanamide [ $\text{Na}^+ \text{N}(\text{CN})_2^-$ ] was reacted with a 68% solution of nitric acid. We chose to use the sodium cation to minimize the production of reaction products by reactions of the cation. The diluted acid allowed reaction to proceed without leading to an ignition event so that products of the reaction could be studied.

The gas-phase reaction products were sampled using a quartz microprobe and the products were analyzed using a triple quadrupole mass spectrometer. When possible, the product species were calibrated using certified calibration gases. In these experiments, approximately 100mg of sodium dicyanamide was loaded into an aluminum reaction vessel. Aluminum was used because it is relatively inert with nitric acid. The acid was delivered to the sample using a syringe pump. Typically 0.2 ml of acid was delivered, which corresponded to the addition of 10 or 11 drops of acid.

Experiments were run to verify the stoichiometry of the overall reaction, suggested by Chambreau et al.<sup>8</sup>



The final set of experiments were conducted to confirm the positive biuret test from the reaction products. In addition, a small sample of dinitrobiuret was obtained from the Klapotke group so that the biuret test could be run on a sample known to contain dinitrobiuret.

Because diluted nitric acid was used, the reaction did not lead to ignition. However, a clear ‘puff’ of white vapor was observed when the acid hit the sodium dicyanamide. The sample also bubbled vigorously. The residual remaining after a test was a white solid. Testing often resulted in the deposition of white crystals on the probe, which sometimes caused the probe to become blocked. A water rinse was effective in opening the probe indicating that the crystals were water soluble. The most likely composition of the crystals appears to be sodium nitrate, consistent with the overall reaction suggested by Chambreau et al.

Initial testing was done to determine the major products of reaction, using low electron energy (22 or 27 eV) to minimize fragmentation of the products. A representative mass spectrum from these experiments is presented in Figure 21. The inset in Figure 21 is from a higher sensitivity test to show the peaks above  $m/z=44$  more clearly. The dominant peak has  $m/z=44$  corresponding to  $\text{N}_2\text{O}$  and  $\text{CO}_2$ . Smaller peaks are observed at 63 and 46, corresponding to nitric acid and  $\text{NO}_2$ , which may be a product of fragmentation of the nitric acid. The remaining peaks that consistently appeared in these tests are at

$m/z=43$  and  $61$ .  $m/z=43$  is small, typical signal levels are 5% or less of the  $m/z=44$  peak. The  $m/z=61$  corresponds to carbamic acid,  $\text{H}_2\text{NCOOH}$ , which could form from reaction of  $\text{HNCO}$  and water. Additional testing was done at higher sensitivity in an attempt to find other trace products; the detection limit under these conditions is approximately 500ppm. Searches for  $\text{N}_2$ ,  $\text{NH}_3$ ,  $\text{HNCO}$ ,  $\text{HCN}$ , and  $\text{NCNH}_x$  compounds were all negative. Thus, the major products have  $m/z=44$  consistent with the observations of Chambreau et al..

The next set of testing was conducted to determine the composition of the  $m/z=44$  peak. The expected product ratio from Reaction R4 is 1.5 moles of  $\text{N}_2\text{O}$  for each mole of  $\text{CO}_2$ . The ratio of  $\text{N}_2\text{O}$  to  $\text{CO}_2$  in the gas-phase products was tested using both parent and ‘daughter’ ions. For the tests using parent ions, the electron energy was set to 70 eV and the ions at  $m/z=30$  and  $44$ . The  $\text{N}_2\text{O}$  mole fraction was determined directly from the  $m/z=30$  peak, then its contribution to the  $m/z=44$  peak was subtracted from the total peak area. The remaining area was then used to determine the amount of  $\text{CO}_2$ . Figure 22 shows that this ratio is fairly constant throughout the course of the reaction. Over the period when signal levels are the strongest, from 65 to 95 seconds, the  $\text{N}_2\text{O}$  to  $\text{CO}_2$  ratio is 1.25. This value matches the expected value of 1.5 within experiment uncertainty of  $\pm 20\%$ . The multiple peaks in the signal correspond to individual droplets of acid hitting the sample.

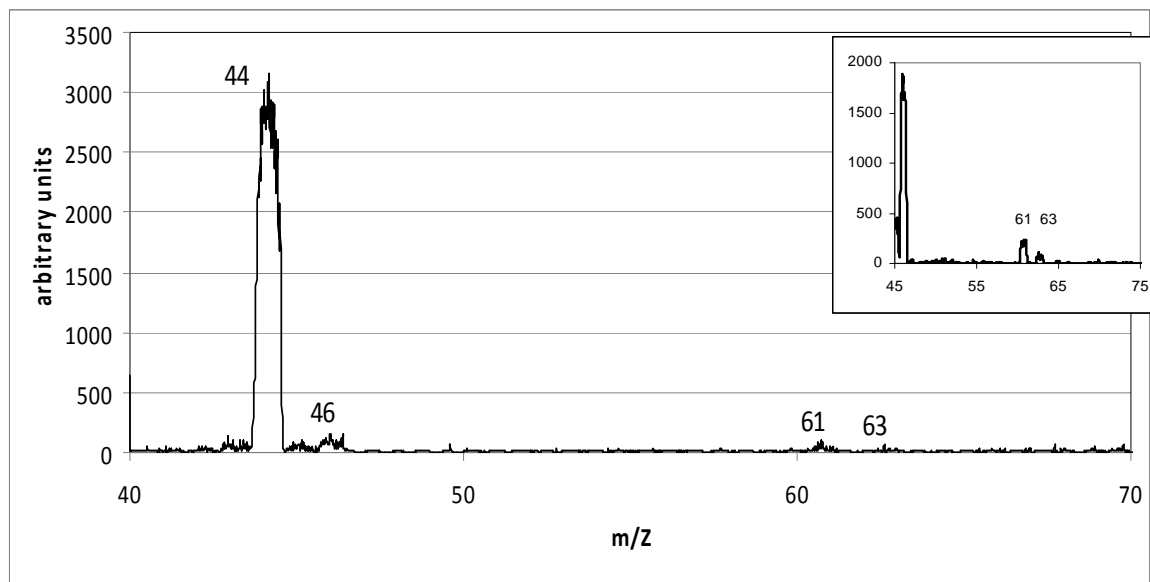


Figure 21: Mass spectrum of products from reaction of sodium dicyanamide with 68% nitric acid solution

Tests were also conducted to see what gases would evolve if the residue were heated. The aluminum vessel was placed on a copper heating plate held at a temperature of  $190^\circ\text{C}$ ; this temperature was chosen based upon the decomposition temperatures reported Geith et al<sup>9</sup>. Almost immediately, signal levels at  $m/z=44$  and  $30$  began to rise, albeit at low signal levels. The ratio was approximately the same as that of

the reaction test indicating that the composition of  $\text{N}_2\text{O}/\text{CO}_2$  was similar to that during the test. No signal was observed at  $m/z=43$ , corresponding to  $\text{HNCO}$ . Thus, if  $\text{HNCO}$  is present in the residue, it must have decomposed into the observed products.

Tests to estimate the overall stoichiometry of the reaction were conducted by observing the sample for evidence of reaction and also by monitoring the evolution of product species. Known masses of sodium dicyanamide, approximately 100 mg, were added to the reaction vessel. The required amount of nitric acid solution was determined based on the reaction stoichiometry in R1. In all tests, the stoichiometric ratio of  $\text{HNO}_3$  to sodium dicyanamide corresponded closely to the expected value of 4. Thus the overall stoichiometry corresponds to the model proposed by Chambreau et al..

The final set of experiments was conducted to determine if a post-reaction sample answered the biuret test. For these tests, the reaction was conducted with the same reactants used by Chambreau et al., sodium dicyanamide and a 34% solution of  $\text{HNO}_3$ . We determined the amount of acid solution required for complete reaction and added that to the sodium dicyanamide. We used a commercial assay test that includes an additive to enhance the sensitivity of the test. For our reaction samples, we did not observe a biuret response. We verified that that assay reagent was working using the test standard provided with the test kit.

Discussions with members of the Edwards team revealed that they had not used a commercial biuret assay, but rather worked the required reagents. The major difference in the procedures turned out to be the amount of acid that was added to the sample. When the pH of the sample was pushed to the levels used by the Edwards team a slight color change was observed in the test samples.

Because Davis and Blanchard<sup>10</sup> reported that nitrobiuret did not give a positive biuret test, we decided to check whether dinitrobiuret would. Fortunately, we were able to obtain a small sample of this material from the Klapotke group. Neither tests in aqueous solution nor pure dinitrobiuret gave a positive biuret test. Therefore, it would appear that something other than biuret is causing the positive response by the test sample. The work of Davis and Blanchard suggests that dicyanic acid is the most likely candidate to explain the positive biuret test.



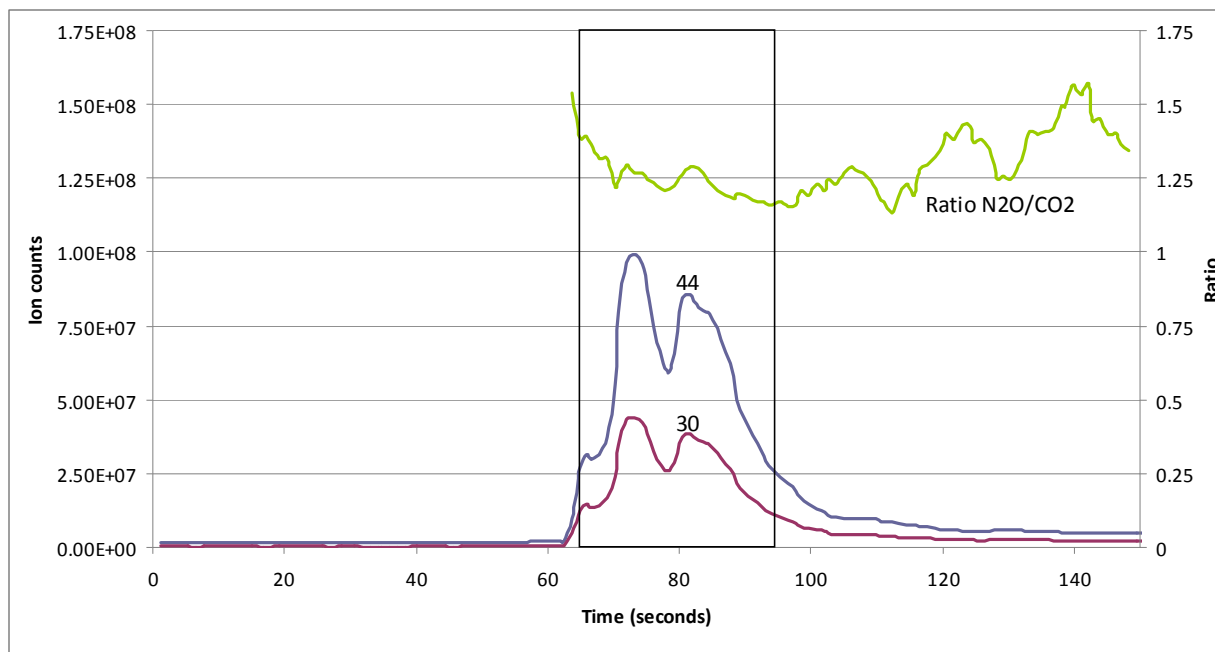
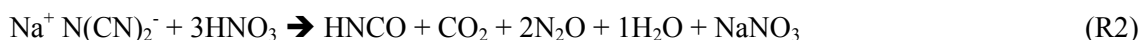


Figure 22: Time evolution of  $m/z=30$  and  $44$  during test along with calculated ratio of  $N_2O/CO_2$

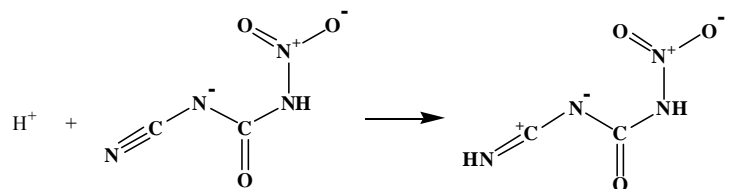
If dicyanic acid is present in the solution, then the molar ratio of  $N_2O/CO_2$  should be larger than 1.5. Each mole of  $HNCO$  will react with one mole of  $HNO_3$  to form one mole of  $N_2O$  and  $CO_2$ . So if the overall reaction were such that one mole of  $HNCO$  is formed as in Reaction R2, the molar ratio of  $N_2O/CO_2$  would be 2, not 1.5.



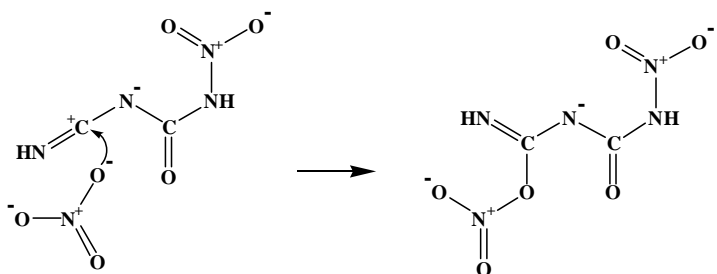
Thus, the ratio of  $N_2O/CO_2$  in our experiments is consistent with the fact that we observed no  $HNCO$  evolving from the post-reaction residue. In addition, our measurement of the overall stoichiometry of the reaction shows that it is close to the 4/1 ratio of R1. This results suggests that little unreacted  $HNCO$  is present in the solution, but it is not possible to say that none is present. It may be present in sufficient amount that it is producing the slightly positive biuret test on the reaction samples.

Given that dinitrobiuret could not be confirmed in the post-reaction products, other potential pathways for reaction can be considered. The studies of Geith et al.<sup>9</sup> and of Davis and Blanchard<sup>10</sup> on the decomposition of nitrobiuret suggest that decomposition of the nitro-substituted intermediate (see R1 below) formed in reactions proposed by Chambreau et al. is also possible. These pathways would lead to the same products as the mechanism proposed by Chambreau et al. So gas-phase measurements alone cannot determine which mechanism is correct. It is possible that both the nitro and dinitro compounds are

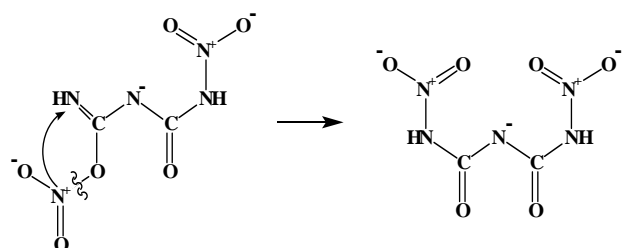
formed during the ignition sequence. But as temperatures increase due to the exothermicity of the reaction, the decomposition of the nitro derivative may accelerate to the point where the dinitroniburet is no longer formed.



R3



R4



R5

### 3.3.3 Investigations of hypergolic ignition chemistry using Confined Rapid Thermolysis

The species evolution profiles at three different temperatures extracted after averaging a multitude of tests for the purpose of optimizing the reaction rate parameters are displayed in Fig. 23. Since quantification of HNCO in terms of mole fractions is a tedious job, it has been left out of the species list. Also, H<sub>2</sub>O has been excluded due to the presence of 30% water in nitric acid, which however, increases the probabilities of third body reactions in the condensed phase.

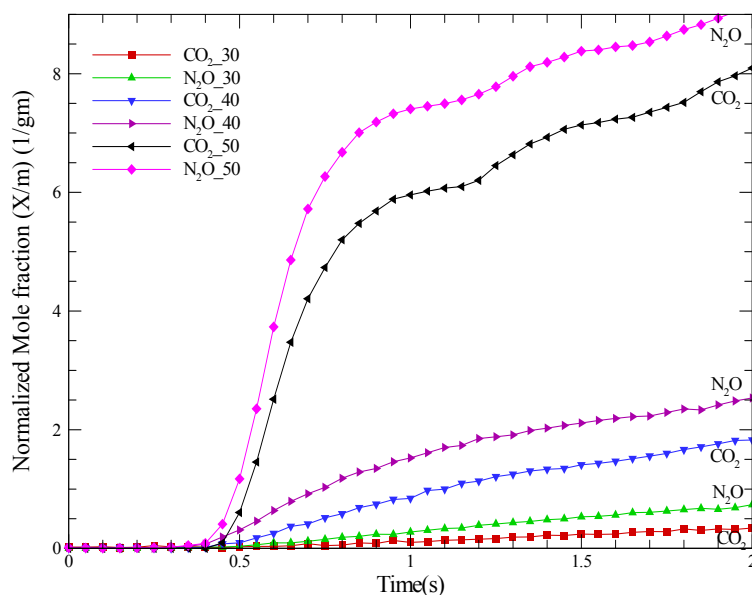


Figure 23: Species evolution from hypergolic reaction of EmimDCA with 70% HNO<sub>3</sub> at 30, 40, and 50°C and 1 atm N<sub>2</sub>.

In order to further elaborate on the reactions leading to the formation of N<sub>2</sub>O and HNCO among the final products, EmimDCA was brought in contact with 40% H<sup>15</sup>NO<sub>3</sub> at 90°C. A representative spectrum obtained from the gas phase is displayed in Fig. 9.10. The principal rovibrational band at 2225 cm<sup>-1</sup> due to N<sub>2</sub>O was found to be shifted to a lower wavenumber. The bands in the spectrum corresponding to N<sub>2</sub>O were found to be due to <sup>14</sup>N<sup>15</sup>NO, thus proving that the –NO functionality in N<sub>2</sub>O is derived from HNO<sub>3</sub>. The peak at 2270 cm<sup>-1</sup> due to HNCO was found to be unaffected by the presence of the isotopic nitrogen, showing that the nitrogen on HNCO is derived from the dicyanamide anion.

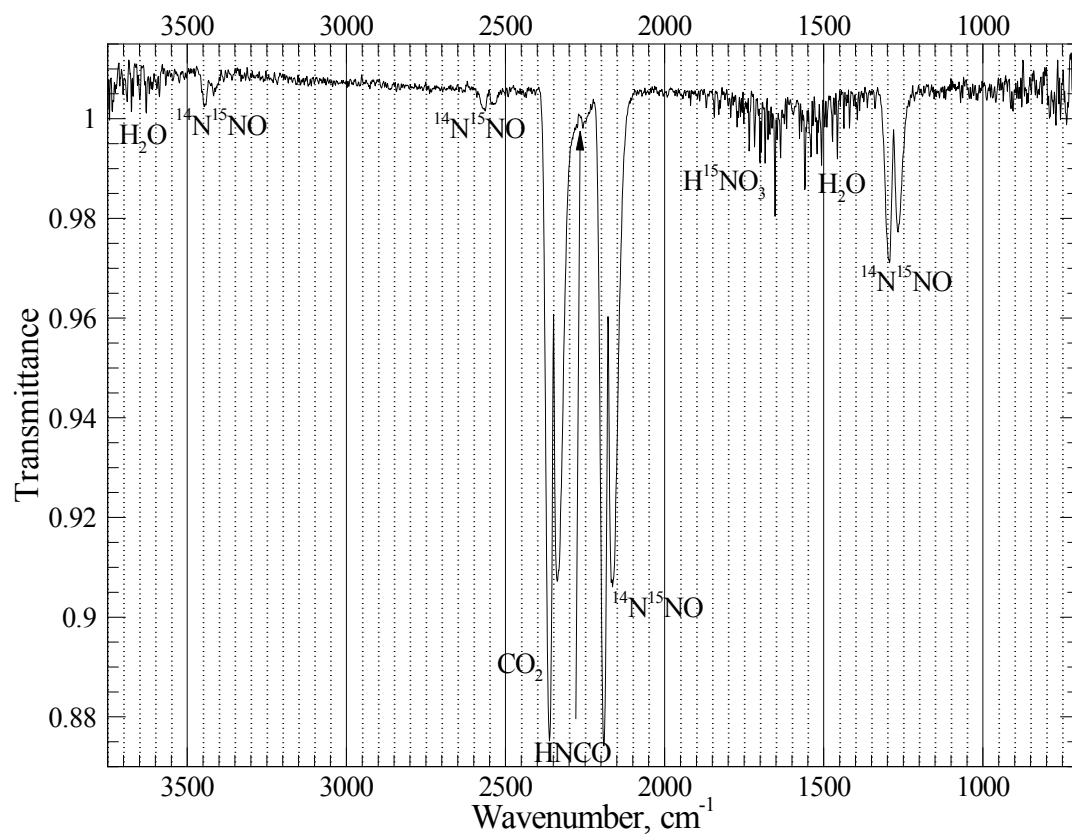


Figure 24: FTIR spectrum of species from hypergolic reaction of EmimDCA with 40% H<sup>15</sup>NO<sub>3</sub> at 90°C and 1 atm N<sub>2</sub>.

## References

---

- <sup>1</sup> Kim, E. S.; Lee, H. S.; Mallery, C. F.; Thynell, S. T., “Thermal decomposition studies of energetic materials using confined rapid thermolysis / FTIR spectroscopy,” *Combustion and Flame*, Vol. 110, No. 1-2, 1997, 239.
- <sup>2</sup> Mallery, C. F.; Thynell, S. T., “Species and Temperature Profiles of Propellant Flames Obtained from FTIR Absorption Spectrometry,” *Combustion Science and technology*, Vol. 122, 1997, 113.
- <sup>3</sup> Linstrom, P. J.; Mallard, W. G., Eds., *NIST Chemistry WebBook, NIST Standard Reference Database Number 69*. National Institute of Standards and Technology, Gaithersburg MD, 20899, 2005.
- <sup>4</sup> Bobeldijk, M., W.J., Van der Zande, and P.G., Kistemaker, “Simple Models for the Calculation of Photionization and Electron Impact Ionization Cross Sections of Polyatomic Molecules,” *Chemical Physics*, Vol. 179, 1994, 125.
- <sup>5</sup> Y.I. Rubtsov, A.I. Kazakov, S.Y. Morozkin, L.P. Andrienko, Zh. Prikl. Khim. 57, 1984, 1926.
- <sup>6</sup> G. Fischer, G. Holl, T.M. Klapötke, J.J. Weigand, *Thermochim. Acta* 437(1-2) (2005) 168.
- <sup>7</sup> T. Shimanouchi, J. Phys. Chem. Ref. Data 6 (1977) 993.
- <sup>8</sup> S. Chambreau, S. Schneider, M. Rosander, T. Hawkins, C. Gallegos, M. Pastewait, G. Vaghjiani, *Journal of Physical Chemistry A*, 112 (2008), 7816
- <sup>9</sup> J Geith, G. Holl, T. M. Klapotke, J. J. Weigand, *Combustion and Flame* 139 (2004) 358
- <sup>10</sup> T. L. Davis and K. C. Blanchard, *J. Am. Chem. Soc.*, 51(6) (1929) 1806

### **Personnel Supported over duration of grant**

Faculty: Tom Litzinger, Stefan Thynell

Research Technician: Larry Horner

Graduate Students: Arin Chowdhury, Pnkaj Jha

Post-doctoral Scholars: Jianquan Li, Suresh Iyer

### **Publications over duration of grant**

#### **Archival:**

Litzinger, T. A. and Iyer, S. S., Hypergolic Reactions of Dicyanamide-based Ionic Liquids with Nitric Acid, submitted to Energy and Fuels, August 2010.

Chowdhury, A. and Thynell, S. T., Confined rapid thermolysis/FTIR/ToF studies of methyl-amino-triazolium-based energetic ionic liquids, accepted for publication in Thermochemica Acta.

Chowdhury, A. and Thynell, S. T., Kinetics of decomposition of energetic ionic liquids, accepted for publication in Propellants, Explosives, Pyrotechnics.

Chowdhury, A., Bapat C., and Thynell, S. T., Apparatus for probing pre-ignition behavior of hypergolic materials, Review of Scientific Instruments, 80(4), 2009.

Chowdhury, A. and Thynell, S. T., Confined rapid thermolysis/FTIR/ToF studies of tetrazolium-based energetic ionic liquids, Thermochemica Acta, 485(1-2), 2009, pp. 1-13.

Chowdhury, A. and S. T. Thynell, Confined rapid thermolysis/FTIR/ToF studies of triazolium-based energetic ionic liquids, Thermochemica Acta, 466, 2007, 1-12.

Li, J. and Litzinger, T. A., Thermal decomposition of 4-amino-1,2,4-triazolium nitrate under infrared laser heating,” Thermochemica Acta, Volume 454, 2007, 116-127.

#### **Meeting Proceedings:**

Chowdhury, A., Thynell, S. T., and Wang, S., “Ignition Behavior of Novel Hypergolic Materials,” 45th AIAA/ASME/SAE/ASEE Joint Propulsion Conference & Exhibit, Denver, August 3-5, 2009.

Litzinger, T.A. and S. Iyer, Reaction Mechanism for Hypergolic Ignition of Dicyanamide-based Ionic Liquids, Proceedings of the Fall Technical Meeting of the Eastern States Section of the Combustion Institute, College Park, MD, October 18-21, 2009, 6 pp.

#### **Interactions/Transitions over Course of the Grant**

We had continuing interactions the ionic liquids group of AFRL at Edwards including transfer of materials to our labs for testing. Interacted with Edwards group on mechanism of hypergolic ignition to determine the reason for differences in experimental results of the two groups.

We had substantive interactions with Mark Gordon and Mike Schmidt of Iowa State regarding molecular modeling of the reactions of ionic liquid.

Jean'ne Shreeve provided a series of compounds for our project.

#### **New Discoveries/Inventions/Patent Disclosures**

None to report

#### **Honors and Awards**

Thynell: Fellow of ASME, Associate Fellow of AIAA

Litzinger: Fellow of ASEE